Response to comments from Reviewer 2

We would like to thank the reviewer for their careful reading of this manuscript. All these minor comments have been remedied as detailed below.

Reviewer comments are given in green, authors reply in black and revised text sections included in blue italics. The revised manuscript and figure captions are appended to this reply highlighting all changes made, and including updated versions of the figures.

line 57. Drewry 1970 is missing from the reference list.

This has now been added.

line 74. Change Carol to Carroll.

Done

line 80. Fassnacht et al 2009. Do you mean 2009a or 2009b?

Now specifies Fassnacht et al., 2009b

line 85. Change "surface" to "survey".

Done

line 100. Fassnacht et al 2010 is not in the reference list.

Sorry, ought to have been 2009a, and now has been corrected.

line 104-105. Change "Mankoff et al." to "Mankoff and Russo". Also on lines 165 and 455.

Corrected in all 3 places

lines 107-109. This sentence will be easier to read if written with parallel construction. Change to "(i) to perform the first . . . (ii) to perform an examination . . . (iii) to compare the volume . . ."

Now reads: "*The method of DSM generation is evaluated against standard terrestrial laser scanning, and the Kinect-derived DSMs of the penitentes are used to (i) perform the first detailed examination of the morphometry of natural penitentes over the course of an ablation season; (ii) compare the volume change computed from DSM differencing with estimates based on manual measurements of surface lowering and (iii) examine the geometrical roughness properties of the sampled penitente surfaces.*"

line 114. Change "mas" to "mass"

Done

line 121. Change "Figure 1b" to "Figure 1"

Done, and we also reference this figure for the other site features described.

line 267. Change Brutseart to Brutsaert.

Done

line 357. "strong east-west preferential orientation". But Figures 4e and 4f show aspect orientation north-south, not east-west. You need to define "aspect".

Now reads: "*The morphometry of the sampled penitentes changed visibly over the measured intervals (Figures 3 and 4). The strong east-west lineation and preferred north and south surface aspect predicted from theory developed early and was maintained throughout study period.*"

line 382. Change Lettaus to Lettau's

Done

line 401. "at site A". Figure 8 caption mentions only site B, not site A.

The sentence is not intended to refer to Figure 8. We have added the missing reference to Table 3 here that shows the change in calculated roughness properties over time.

line 409. "predominantly from the south-westerly sector". On Figure 9 the wind direction is predominantly SE not SW.

Correct! This now reads: "*Over the whole study period wind direction is predominantly from the south-easterly and north-westerly sectors, and swings through both extreme wind angles used in the roughness calculations here (Figure 9).*"

lines 522-525. This is an important result; it should be included in the abstract.

Abstract now includes: "*Morphometric analysis shows that skimming flow is persistent over penitentes, providing conditions conducive for the development of a distinct microclimate within the penitente troughs.*", and has been substantially shortened in response to comments from R1.

line 674. Breidamerkurjökull. (change h to k)

Done

line 682. Change "roughness of" to "roughness on"

Done

Table 2. Units of windspeed should be m/s. So change the exponent from -2 to -1.

Done

Table 3. This table is not referenced in the text.

Thank you. We now refer to this table as follows: "*Table 3 shows the calculated roughness values at each survey date, revealing that while profile-computed roughness length increases monotonically over time at site B, it reduces over the first period at site A, associated with snowfall during this period.*"

Figure 1. What are the units of the tick labels? They should be replaced with latitude and longitude, or else removed.

They were in UTM and have now been replaced with latitude and longitude

This has been done

In Figure 4 the heights are all plotted relative to the reference height of the uppermost stake marking out the horizontal reference for manual measurements of surface lowering. This is described in both the text and the figure caption: "*Figure 4: Summary of the DSM properties through time at site A (left) and B (right). Surface height distribution as a percentage of total surface area, in local coordinates [m] relative to the position of the northern end of ablation frame (a & b). Inset tables show weighted mean mesh elevation, range, surface area and surface area as a function of the horizontal area of the sampled site. Distribution of surface angles as a percentage of total surface area (c & d). Aspect distribution as a percentage of total surface area (e & f).*"

The colors refer to dates and these are now labelled on the figure. The height coordinate is relative to the NE corner marker of site A, and the caption now reads: "*Figure 9: Examples of (a) N-S, and (b) E-W oriented cross sections sampled at 0.1 m intervals in local coordinates at site B from which effective surface roughness properties were computed using the methods of Munro (1989, 1999).The surface height coordinate is relative to the NE corner marker of site A.*"

3D surface properties of glacier penitentes over an ablation season, measured using a Microsoft Xbox Kinect.

~~L~~Lindsey. I. Nicholson[1], ~~M~~Michał. Pętlicki[2,3], ~~B~~Ben. Partan[4], and ~~S~~Shelley. MacDonell[3]

[1] *Institute of Atmospheric and Cryospheric Sciences, University of Innsbruck, Innsbruck, Austria*
[2] *Institute ~~for~~of Geophysics, Polish Academy of Sciences, ul. Księcia Janusza 64, 01-452 Warsaw, Poland*
[3] *Centro de Estudios Avanzados en Zonas Áridas (CEAZA), La Serena, Chile*
[4] *University of Maine, Orono, USA*

~~Correspondance~~Correspondence to: L. I. Nicholson (lindsey.nicholson@uibk.ac.at)

Abstract. ~~Penitentes are a common feature of snow and ice surfaces in the semi-arid Andes where very low humidity, in conjunction with persistently cold temperatures and sustained high solar radiation favour their development during the ablation season. As penitentes occur in arid, low latitude basins where cryospheric water resources are relatively important to local water supply, and atmospheric water vapor is very low, there is potential value in understanding how penitentes might influence the runoff and atmospheric humidity.~~

~~The complex surface morphology of penitentes makes it difficult to measure the mass loss occurring within them because the (i) spatial distribution of surface lowering within a penitente field is very heterogeneous, and (ii) steep walls and sharp edges of the penitentes limit the line of sight view for surveying from fixed positions and (iii) penitentes themselves limit access for manual measurements.~~ In this study, ~~we solved these measurement problems by using a Microsoft Xbox Kinect sensor to generate~~the first small-scale digital surface models (DSMs) of ~~small sample areas of snow and ice~~natural penitentes on a glacier surface were produced using a Microsoft Xbox Kinect sensor on Tapado Glacier ~~in~~, Chile (30°08'S; 69°55'W~~ between November 2013 and January 2014.~~). The surfaces produced by the complete processing chain were within the error of standard terrestrial laser scanning techniques~~. However, in our study,~~ but insufficient overlap between scanned sections that were mosaicked to cover the ~~studied sites~~sampled areas can result in three-dimensional positional errors of up to 0.3 m.

~~Mean surface lowering of the scanned areas was comparable to that derived from point sampling of penitentes at a minimum density of 5 m^{-1} over a 5 m transverse profile. Over time the~~Between November 2013 and January 2014 penitentes become fewer, wider, deeper, and the distribution of surface slope angles becomes more skewed to steep faces. ~~These~~Although these morphological changes cannot be captured by ~~the interval sampling by~~ manual point measurements~~.~~, mean surface lowering of the scanned areas was comparable to that derived from manual measurements of penitente surface height at a minimum density of 5 m^{-1} over a 5 m transverse profile. Roughness was computed on the 3D surfaces by applying two previously published geometrical formulae; one for a 3D surface and one for single profiles sampled from the surface. Morphometric analysis shows that skimming flow is persistent over penitentes, providing conditions conducive for the development of a distinct microclimate within the penitente troughs. For each method a range of ways of defining the representative roughness element height ~~required by these formulae~~was used, and the calculations were done both with and without ~~using~~application of a zero displacement height offset to account for the likelihood of skimming air flow over the closely-spaced penitentes. The computed roughness values are in the order of 0.01-0.10 m during the early part of the ablation season, increasing to 0.10-0.50 m after the end of December, in line with the roughest values previously published for glacier ice. Both the 3D surface and profile methods of computing roughness are strongly dependent on wind direction. However, the two methods contradict each other in that the maximum roughness computed for the 3D surface coincides with airflow across the penitente lineation while maximum roughness computed for sampled profiles coincides with airflow along the penitente lineation. These findings highlight the importance of determining directional roughness and wind

43 direction for strongly aligned surface features and also suggest more work is required to determine appropriate
44 geometrical roughness formulae for linearized features.

1. Introduction

46 Penitentes are spikes of snow or ice, ranging from a few centimetres up to several metres in height that can form
47 during the ablation season on snowfields and glaciers ~~under the right conditions. The conditions required for~~
48 ~~penitentes to form~~. They are ~~dew point below 0°C, persistently low air temperatures and sustained strong solar~~
49 ~~insolation (Lliboutry, 1954). These conditions are frequently met at~~a common feature of high elevation, low-latitude
50 glaciers and snowfields~~, such as in the subtropical Andes~~ (e.g. Hastenrath and Koci, 1981; Corripio and Purves,
51 2005; Winkler et al., 2009~~),~~) where ~~penitentes are widespread during the ablation~~very low humidity, persistently
52 cold temperatures and sustained high solar radiation favour their development (Lliboutry, 1954). As cryospheric
53 water resources are relatively important to local dry season~~–~~ water supply in arid mountain ranges (Kaser et al.,
54 2010), there is potential value in understanding how penitentes might influence both runoff and atmospheric
55 humidity.

56 ~~Observations show that penitente~~Penitentes form linearized, inclined fins of snow or ice on the surface. Both the
57 latitudinal range (within 55° of the equator on horizontal surfaces) and geometry ~~is~~ (aligned with the arc of the sun
58 across the sky, and tilted toward the sun at local noon~~, highlighting the importance~~) of penitentes are governed by
59 solar~~ radiation in penitente formation~~-to-surface geometry (Lliboutry, 1954; Hastenrath and Koci, 1981; Bergeron et
60 al., 2006~~). Indeed, the alignment and restricted latitudinal range of penitentes (within 55° of the equator on~~
61 ~~horizontal surfaces) can be explained by solar to surface geometry alone (~~; Cathles et al., 2014). ~~The process~~During
62 the initial stages of penitente ~~growth involves geometric focusing of incident solar radiation~~ development, ablation is
63 thought to proceed by ~~surface~~sublimation alone driven by the low atmospheric humidity. Surface irregularities ~~that~~
64 ~~causes~~focus reflected solar radiation within depressions ~~to receive more radiation than surrounding peaks~~ (Amstutz,
65 1958; Corripio and Purves, 2005; Lhermitte et al., 2014; Claudin et al., 2015~~). Consequently, ~~) such that the energy
66 receipts, and consequently ablation, are ~~initially~~enhanced in the hollow ~~due to multiple reflection of irradiance, ~~and
67 the surface irregularity becomes amplified. ~~However for substantial penitente growth it is crucial that, at the tips of~~
68 ~~penitentes, ablation occurs by sublimation and the snow/ice temperature remains below the melting point, while in~~
69 ~~the troughs between penitentes, melting can occur once~~Subsequently, as the surface relief increases, a more humid
70 microclimate is ~~established within the hollow~~thought to develop in the hollows between penitentes, supressing
71 sublimation and allowing melting in the depressions. Meanwhile, the penitentes tips continue to ablate by
72 sublimation alone (Lliboutry, 1954; Drewry, 1970; Claudin et al., 2015~~). Once the snow/ice in the hollows has~~
73 ~~reached the melting point, the spatial differentiation of ablation processes serves to further amplify the penitente~~
74 ~~relief as melting only~~) and, as melting requires approximately an eighth of the energy of sublimation to remove the
75 same amount of ice, the spatial differentiation of ablation process between penitente trough and tip is very effective
76 at amplifying the penitente surface relief.

77 The altered partitioning of ablation between sublimation and melting that occurs in penitente fields, as compared to
78 surfaces without penitentes (e.g. Lliboutry, 1998; Winkler et al., 2009; Sinclair and MacDonell, 2015~~The impact of~~
79 ~~penitentes on the surface energy balance and ablation of snow and ice is of interest in arid mountains catchments,~~
80 ~~where penitentes are widespread and meltwater can be a substantial contribution to local hydrological resources~~
81 ~~(Kaser et al., 2010). Previous studies have shown that penitentes alter the surface energy balance of snow and ice~~
82 ~~surfaces by reducing~~), is expected to alter the rate of mass loss and meltwater production of snow and icefields
83 during the ablation season, but this has not yet been fully quantified. Previous studies, based on modelling idealized
84 penitente surfaces, have investigated the impact of penitentes on the shortwave radiative balance, and suggest that
85 penitentes reduce effective albedo by up to 40% compared to flat surfaces (Warren et al, 1998; Corripio and Purves,
86 2005; MacDonell et al., 2013; Cathles et al., 2014; Lhermitte et al., 2014~~) as well~~). In addition to altering the
87 ~~partitioning of ablation between sublimation and melting (e.g. Lliboutry, 1998; Winkler et al., 2009; Sinclair and~~

MacDonell, 2015). Thus, the presence of penitentes is expected to alter the rate of mass loss and meltwater production of snow and icefields during the ablation season, and, on the basis of the radiative balance it has been postulated that they will accelerate the snow and ice mass loss rates (Cathles et al., 2014). Howeverproperties of the surface, the development of penitentes on the surface will also alter the roughness properties in both space and time, but this, as well as its impact on the resultant turbulent fluxes is not quantified. The wind direction dependence of manifestly alters the surface roughness properties, but neither the impact of penitentes on surface roughness, nor the associated impact on turbulent energy fluxes has been investigated. The roughness of snow and ice surfaces is particularly prone to varying in space and time (e.g. Smeets et al., over linearized surface features has been previously observed in wind1999; Brock et al., 2006; Fassnacht et al., 2009b). Wind profile measurements over snowlinearized sastrugi, for which surface features shows that the derived aerodynamic roughness length varied from 1--70 mm over a 120° range of impinging wind direction (Jackson and CarolCarroll, 1978). While penitentes are a relatively rare form of linearized surface feature in many glacierized environments, in contrast, linear crevasses are widespread, and although the impact of wind direction on roughness and the resultant turbulent heat fluxes is generally not treated in glaciology, penitentes offer a unique test bed for investigating the significance of linearized features on effective surface roughness for various wind directions.

In general, the physical roughness of snow and ice surfaces are particularly prone to varying in space and time (e.g. Smeets et al., 1999; Brock et al., 2006; Fassnacht et al., 2009), it is desirable to be able to replace relatively logistically and technologically challenging methods of determining roughness parameters from atmospheric profile or eddy covariance measurements, with methods based on more readily measurable surface terrain properties (e.g. Kondo and Yamazawa, 1986; Munro, 1989; Andreas, 2011), or properties such as radar backscatter that can be derived from spaceborne instruments (e.g. Blumberg and Greeley, 1993). The most comprehensive surface of methods to determine apparent aerodynamic properties from surface morphometry was carried out by Grimmond and Oke (1999) who tested several methods in urban environments, which are among the roughest surface conditions encountered in boundary layer atmospheric studies. The morphometric estimates of roughness properties were compared with those from aerodynamic methods from numerous field and laboratory studies. Many of the aerodynamic studies were found to be flawed, and the study demonstrates that, despite the considerable effort in obtaining such measurements, their reliability in complex and rough terrain is contested as the computations rely upon theory that is developed for flat homogenous terrain, and in general the aerodynamic results show a similar amount of spread as the various geometrical methods tested. Although, Grimmond and Oke (1999) consider that direct measurements of fluxes over complex terrain are most likely the 'best' way of determining surface properties, the difficulties of deploying the expensive and relatively delicate instruments over glacier surfaces makes a geometric determination even more appealing. However, in the case of penitentes, such studies are impeded by a scarcity of information on real penitente geometry.

Measurements of natural penitentes (e.g. required to examine their morphometry and roughness are rare (e.g. Naruse and Leiva, 1997) are rare as they are generally found in relatively inaccessible areas and the complex surface relief poses a considerable impediment to movement and measurement, for example preventing), and difficult to obtain because the complex, and partially overhanging, surface prevents the use of simplified automated tools such as photogrammetric determination of surface profile heights (e.g. Fassnacht et al., 20102009a; Manninen et al., 2012). Furthermore, accurately measuring the convoluted penitente surface is in itself a significant challenge, as it includes overhanging surfaces, which is problem for immobile) or line-of-sight surveying equipment. However,from fixed positions. Recent advances in close-range mobile depth-of-field sensors and efficient feature tacking software used in interactive computer gaming offer potentially useful tools that can be applied to generate small scale digital surface models to resolve such problems in earth science (e.g. Mankoff et al.,and Russo, 2013). In this study sample plots of penitentes in snow on a glacier surface are scanned using a Microsoft Xbox Kinect sensor is used as a close-range mobile distance ranger to produce a series of small-scale digital surface models (DSMs). These surface models are used to perform (i) The method of DSM generation is evaluated against standard terrestrial laser scanning, and the Kinect-derived DSMs of the penitentes are used to (i) perform the first detailed examination of the

~~geometry~~morphometry of natural penitentes ~~and how they change~~ over the course of ~~the core~~an ablation season; (ii) ~~an examination of the geometrical roughness properties of penitentes and (iii)~~ compare the volume ~~changes~~change computed from DSM differencing ~~the DSMs~~ with ~~the volume changes estimated from~~estimates based on manual measurements of surface lowering ~~within a penitente field. These measurements enable evaluation of how accurately simplified~~and (iii) examine the geometrical roughness properties of the sampled penitente surfaces ~~used in theoretical modelling represent the true surfaces found in nature, improved parameterization of surface roughness in energy balance models applied to glacier and snowfields with penitentes, and the performance of energy balance models over penitente surfaces to be evaluated against mas loss derived from the measured surface changes~~.

2. Methods

2.1 Description of fieldsite

Tapado Glacier (30°08'S; 69°55'W) lies in the upper Elqui Valley of the semi-arid Andes of the Coquimbo Region of Chile (Figure 1). ~~This~~The glacier is relatively ~~easily~~accessible and ~~previous research indicates that the glacier surface develops~~is known to develop penitentes every summer (Sinclair and MacDonell, 2015). Two separate study areas were analysed. Firstly, a test site was established at a patch of snow penitentes within a dry stream bed at 4243 m a.s.l. in the glacier foreland (Figure ~~1b~~1). This site was used to (i) ~~trial~~test instrumental setups in order to optimize the field operation of the Kinect sensor, and (ii) compare the performance of the Kinect sensor against a Terrestrial Laser ~~Scanning~~Scanner (TLS~~) system~~.~~.~~). This location was chosen due to the logistical difficulties of transporting the TLS to the glacier. Subsequently, two study plots were established at an elevation of 4774 m a.s.l. ~~within~~on the glacier ablation zone~~.~~ (Figure 1). These ~~surfaces at these~~sites were ~~measured~~scanned repeatedly ~~using~~with the Xbox Kinect (see section 2.3) during the core ablation season between the end of November 2013 and the beginning of January 2014. ~~An automatic weather station on a free-standing tripod was installed beside the two plots to provide meteorological context for the measurements.~~

The location and layout of the two glacier sites is shown in Figure ~~1~~1a. Site A (5 m by 2 m) was measured four times, on 25 November, 11 December, 20 December and 3 January. Site B (2 m by 2 m~~, Figure 1c~~) was only measured on the last three dates~~(Figure 1c)~~.~~.~~ The corners of the study sites were marked with 2 m lengths of plastic plumbing piping hammered vertically into the snow, or drilled into the ice~~.~~ (Figure 1c). In order to locate the study sites in space and to provide a common reference~~frame~~ for each survey date, marker stake positions were measured using a Trimble 5700 differential GPS with Zephyr antenna on the 25th November, with a base station in the glacier foreland. On each visit to the glacier, when possible, the stakes were hammered further into the snow and the resultant lowering of the stake top was noted. The maximum standard deviations of the GPS stake positions were < 1.0 cm, 1.1 cm and 1.7 cm in easting, northing and elevation respectively, with combined XYZ standard deviation < 2.0 cm for all stakes (Supplement A). Error on the manual measurements of height offsets of the marker stakes on subsequent survey dates is conservatively estimated to be 2.0 cm. This results in total positional errors of the ground control points at each scan date of between 2.3 and 2.7 cm depending on the stake. Manual measurements of surface lowering were made along the eastern long side of site A. All surfaces heights were referenced to the elevation of the glacier surface at the upglacier end of this cross profile at the date of installation. An automatic weather station (AWS) on a free-standing tripod was installed beside the two glacier plots to provide meteorological context for the measurements (Figure 1).

2.2 Terrestrial laser scanning

~~Surface scans of snow penitentes at~~At the test site ~~were undertaken with both a terrestrial laser scanner (TLS) and the Kinect sensor in order to compare the~~ surface scans produced by the ~~well established TLS method and the~~ relatively new Kinect sensor ~~application~~were compared with those produced by the well-established TLS method. The TLS system used was an Optech ILRIS-LR scanner, which is a long-range terrestrial laser scanner especially

4

178 suitable for surveying snow and ice surfaces ~~thanks to~~as it has a shorter wavelength laser beam (1064 nm) than other
179 models. This equipment surveys surface topography based on time-of-flight measurement of a pulsed laser beam
180 reflected to a given angle by a system of two rotating mirrors. It has a raw range accuracy of 4 mm at 100 m
181 distance, raw angular accuracy of 80 µrad, beam diameter of 27 mm at 100 m distance and beam divergence of 250
182 µrad. The instrument was placed in five locations around the surveyed snow patch and boulder, overlooking it from
183 different directions. Positions of the TLS were measured with ~~the~~ Trimble 5700 differential GPS with Zephyr
184 ~~antenna~~antennae in static mode. Seventeen point clouds were obtained with nominal resolution of 0.11-0.75 cm.
185 Resulting point clouds were corrected for atmospheric conditions (pressure, temperature and humidity) and trimmed
186 with ILRIS Parser software, aligned with Polyworks IMAlign software into a common local coordinate system and
187 georeferenced with differential GPS measurements using Polyworks IMInspect software. The alignment error of the
188 point clouds as estimated by this software is 0.36-0.87 cm and comparison with ground control points gives an error
189 of 5.65 cm. The TLS scan of the snow penitentes is presented as an example of the nature of the DSM that can be
190 obtained within a penitente field using TLS (Figure 2). Unfortunately, the scans of snow penitentes could not be
191 carried out with both the TLS and Kinect on the same day, so direct comparison of the TLS and Kinect scans is
192 instead performed on a reference boulder ~~lying on the ground beside~~within the test site, whose surface is assumed
193 unchanged between different scan dates. ~~The TLS scan of the snow penitentes is presented as an example of the~~
194 ~~nature of the DSM that can be obtained within a penitente field using a TLS (Figure 2).~~

2.3 Kinect ~~scans of~~ surface ~~change~~scanning

196 The Kinect sensor emits a repeated pattern of structured infra-red (IR) beams, and records the pattern distortion with
197 an ~~onboard~~ IR camera. The depth-~~-~~of-~~-~~field calculation is performed via a proprietary algorithm and a distance map
198 is the raw data output. Using the standard calibration the static raw depth field resolution of the Kinect is 1 mm and
199 the ~~Kinect measured~~ distance ~~at the center of the field of view is within 1% of the real distance (Mankoff et al.,~~
200 ~~2013), implying an~~ error ~~of~~is < 1.0 cm at the distance range of the penitente scans~~.~~ (Mankoff and Russo, 2013).

201 For its original gaming usage, the Kinect is in a fixed position and proprietary software uses feature tracking to track
202 the movements of players moving within the field of view of the Kinect. However, the inverse of this workflow can
203 also be applied ~~wherein~~whereby the Kinect sensor is moved interactively around a static surface or 3D body, using
204 the same feature tracking to compute the position of the sensor relative to the object and thereby allowing a point
205 cloud reconstruction of the object ~~to be constructed.~~. In this work we apply the second work flow ~~sampling~~and
206 sample Kinect data using the ReconstructMe™ 2.0 software package. In common with alternative reconstruction
207 packages that are compatible with the Kinect, ReconstructMe™ performs bilateral filtering on the output depth map
208 frame and converts the pixel version of each depth map frame to 3D coordinate maps of vertices and normals. An
209 iterative closest point (ICP) alignment algorithm is then applied frame by frame at three scales to repeatedly rotate
210 and translate the depth field to determine camera position and an aligned surface, giving weighted preference to
211 portions of the surface that are perpendicular to the line of sight. ~~This~~The ReconstructMe™ software has the
212 advantage of producing surface meshes in real-time, so that the operator can ~~visibly~~ check the scan quality and
213 coverage at the time of capture, but the disadvantage that the raw point cloud is not saved and if the real-time
214 tracking is lost a new scan ~~sample~~ must be started.

215 The Xbox Kinect was connected via a 5m powered USB extension cord to an MSI GE60 gaming laptop, powered
216 using a 240V 600W inverter connected to the ~~12V~~ 160Ah 12V battery of the automatic weather station on the
217 glacier. Scans were carried out by two people; one moving the Kinect across the penitente field and the other
218 monitoring the quality of the surface being generated ~~The~~ on screen. In bright conditions, the return IR signal of the
219 Kinect is swamped by natural radiation ~~in bright conditions, and this is especially true over bright, rough~~over snow
220 and ice surfaces, which reflect ~~the~~a high proportion of incident shortwave radiation, and absorb or scatter much of
221 the longwave radiation signal. ~~To solve this~~Therefore, scanning was carried out at twilight or just after nightfall.
222 Sudden movements caused by the operator slipping or the snow compacting underfoot ~~can result~~resulted in the

223 ReconstructMe software losing its tracking of common reference points ~~used to generate the continuous surface~~
224 ~~mesh.~~. Consequently, each study site was scanned in small sections and three to thirteen ~~separate~~overlapping surface
225 meshes were used to cover the area of each study site.

2.4 ~~Mesh processing~~

~~Freely available Meshlab software was used to initially align the~~ **Kinect** surface ~~meshes covering each study site~~
~~using a pairwise alignment procedure.~~ **mesh processing**

229 The full mesh processing procedure using the freely available Meshlab software is presented in Supplement B, and
230 briefly described here. Small surface components, unreferenced and duplicated vertices were removed from the
231 meshes using inbuilt filters. ~~The Meshlab alignment~~The component meshes that cover each sampling date at a single
232 site were aligned using an iterative closest point (ICP) algorithm ~~was applied to objectively optimize the alignment~~
233 ~~and compute~~which distributes the alignment error~~. This alignment procedure uses an ICP algorithm to iteratively~~
234 ~~align the component meshes and distribute the alignment errors~~ evenly across the resultant mosaicked surface mesh.
235 Alignment solutions consistently had mean distributed error < 4 mm (Supplement B). The aligned meshes were
236 flattened into a single layer, remeshed using a Poisson filter and ~~finally~~ resampled to reduce the point density by
237 setting a minimum vertex spacing of 2.5mm.

238 The surface mesh for each scan date was georeferenced in Polyworks software using the known coordinates of the
239 base of the marker stakes at the time of each scan because the upper portions of the symmetrical stakes are often
240 poorly captured by the meshing software. The local elevation zero was set to be the north-east corner of site A. The
241 mismatch evident in the georeferencing step (Table 1) is much larger than the mesh alignment error (Supplement B).
242 ~~stakes are often poorly represented in the scans due to the fact that ReconstructMe™ does not handle symmetrical~~
243 ~~objects well. It proved difficult in some cases to locate the surfaces in space such that the locations of all marker~~
244 ~~stakes were consistent with the ground control points.~~ This is most likely an artifact of a combination of (i) reduced
245 mesh quality at the margins of the component scans and (ii) insufficient overlap between some scan sections
246 producing distortion within the mesh alignment. ~~The mismatch evident in the georeferencing step (Table 1) is much~~
247 ~~larger than the mesh alignment error (Supplement B).~~

248 To eliminate the marker stakes and any data gaps near the margins of the study areas, each surface mesh was sub-
249 sampled within the staked area. The sub-sampled area for site A is a 2.0 by 3.5 m horizontal area (7.00 m^2), and site
250 B is a 1.5 x 1.5 m horizontal area (2.25 m^2) shown in the examples in Figure 3. Mesh vertices and an index file of
251 the vertices comprising each face were exported from Meshlab for subsequent analysis in Matlab software.

2.5 Calculations of surface geometrical properties

253 The geo2d and geo3d toolboxes (available from the Matlab File Exchange) were used ~~in Matlab™~~ to compute the
254 ~~triangle~~face areas and normals of the mesh, from which ~~the~~ surface height distribution, aspect and dip of the
255 sampled surface ~~can be determined~~were calculated, weighted by the ~~triangle~~ratio of each face area ~~as a function of~~to
256 the total surface area of all faces. ~~Volume change between~~As the surfaces ~~was~~contain overhanging parts, DSM
257 differencing cannot be performed by simple subtraction. Instead volumes for all surfaces were computed ~~by~~
258 ~~projecting each triangle area onto~~relative to a baselevel horizontal reference ~~surface.~~. Volumes relative to this
259 horizontal reference for upward-facing triangles were computed column-wise ~~from these projected areas~~, by
260 projecting the area of each triangular face onto the reference surface and using the height coordinate of the triangle
261 centroid as the height dimension for each column. These were summed and volumes for overhanging triangles,
262 calculated in the same way ~~as the up-ward facing volumes~~, were subtracted to derive ~~a~~the total volume between the
263 reference surface and ~~the~~each scanned penitente surface. Successive volumes were subtracted to obtain the volume
264 change over each measurement interval.

2.62.6 Manual measurements of surface change

Traditional single-point stake measurements of glacier surface lowering are unreliable within the inhomogeneous surface of a penitente field. One alternative is to measure surface lowering at intervals along a profile perpendicular to the main axis of alignment of the penitentes. Such a reference was installed along the 5 m-long eastern margin of site A, between two longer corner stakes drilled 3 m into the ice using a Kovacs hand drill. The distance between a levelled string and the glacier surface was measured using a standard tape measure at 0.2 m intervals on 23 November. Subsequent measurements, on the 12 and 21 December and on 4 January, were made at 0.1 m intervals. All measurements were recorded to the nearest centimetre, and the error on each measurement is estimated to be 2.0 cm, which is assumed to capture the error associated with the horizontal position of the measurements along the reference frame and the vertical measurements of the distance to the surface beneath.

2.7 Calculations of geometric surface roughness

The aerodynamic roughness length (z_0) is the distance above the surface at which an extrapolation of a logarithmic windspeed profile under neutral conditions would be extrapolated down throughtowards the surface layer andwould reach zero. Over taller roughness elements the level of action of momentum transfer between the airflow and the surface roughness elements is displaced upwards by a distance, termed the zero-plane displacement (z_d). Above particularly rough surfaces, a roughness sub-layer is formed in the lowest part of the surface layer within which surface roughness elements create a complex 3D flow that is almost chaotic. Where roughness elements are widely spaced, the separated flow over obstacles reattaches to the surface before the subsequent obstacle is reached. More closely packed roughness elements experience a wake interference regime, and in the most densely packed arrays of roughness elements skimming flow occurs (Grimmond and Oke, 1999). At the top of the roughness sublayer individual wakes caused by surface obstacles are smeared out and the flow is independent of horizontal position, and thus, observations at this level represent the integrated surface rather than individual surface obstacles. This level is known as the blending height (z_r). All these properties are dependent on the size and arrangement of surface roughness elements.

As it is logistically challenging to deploy instrumentation to determine roughness parameters from atmospheric profile or eddy covariance measurements on glacier surfaces, efforts have been made to instead use methods based on properties such as radar backscatter (e.g. Blumberg and Greeley, 1993) or more readily measurable surface terrain properties (e.g. Kondo and Yamazawa, 1986; Munro, 1989; Fassnacht et al., 2009a; Andreas, 2011). Grimmond and Oke (1999) tested several methods of determining apparent aerodynamic properties from surface morphometry in urban environments, which are among the roughest surface conditions encountered in the atmospheric boundary layer, and found that morphometric determinations of surface roughness do not clearly underperform in comparison with aerodynamic methods, suggesting that morphometric measurements of roughness are worth pursuing.

There are a number of formulations for deriving z_0 from geometrical measurements. For example, the simplest approach is to take the standard deviation of the surface elevations as a measure of roughness (Thomsen et al., 2015). In this work, the surface meshes were analysed for roughness on the basis of a widely-used relationship established by Lettau (1969), initially developed for isolated, regular obstacles distributed over a plane:

$$z_0 = 0.5\, h \left(\frac{s}{S}\right) \tag{1}$$

where h is the height of the obstacles, s is the upwind silhouette area of each obstacle and S is the specific area occupied by each roughness element obstacle, also referred to as its lot area. The roughness values computed using Equation 1 over 3D snow surfaces has been shown to vary widely depending on the methods of surface interpolation used (Fassnacht et al., 2014), due to the influence on interpolation method on the unit surface area occupied by each roughness element. However in this work the high resolution meshes used can be expected to adequately capture the

308 surface properties as no extrapolation or interpolation procedure is needed. Isolated roughness elements of regular
309 geometry distributed over a horizontal plane are a poor analogy for the irregular surface topography of a penitente
310 field, and the applicability of this formulation over penitentes has not been established. Nevertheless, we apply the
311 analysis as an illustration of the nature of the results generated from such an approach over penitentes and hope that
312 future aerodynamic roughness lengths obtained from micrometeorological measurements can be compared to these
313 ~~geometrically~~ morphometrically-derived ones. Macdonald and others (1998) state that for irregular obstacles h can
314 be replaced by average obstacle height, s with the sum of all the upwind silhouette areas, and S with the total area
315 covered by the obstacles. While the upwind silhouette area, and indeed surface area in any direction, is relatively
316 easily defined for each surface mesh area using trigonometry, it is difficult to define individual roughness elements
317 and their representative heights, due to the lack of an apparent base level. Here we first detrend the surfaces to
318 remove any general surface slope at the site, then compute the roughness for the detrended 3D meshes assuming that
319 the roughness elements cover the whole surface area (i.e S = plot area), and for four possible representations of
320 average obstacle height (h) as follows: (i) the maximum range of the detrended mesh; (ii) twice the standard
321 deviation of the detrended surface mesh; (iii) mean mesh height above the mesh minimum; and (iv) median mesh
322 height above the minimum.

323 These data are computed for illustrative purposes only as it is reported that Equation 1 fails when the roughness
324 element density exceeds 20-30~~%,~~% (Macdonald et al., 1998), as is expected for penitente fields ~~(Macdonald et al.,~~
325 ~~1998)..~~ High density roughness elements means that they interfere with the airflow around each other, and upwards
326 displacement of the zero wind velocity level ~~is displaced upwards, and~~means that effective roughness is a result of
327 the roughness elements above this zero velocity displacement plane.~~ The~~, and the zero displacement height~~ in this~~
328 ~~sense~~, gives an indication of the penetration depth of effective turbulent mixing into the penitente field. Accordingly,
329 we additionally present sample calculations of three-dimensional roughness on the detrended surface meshes using
330 three possible realizations of z_d, as, like h, z_d is also unknown in the case of the penitente fields being sampled. In
331 the first case, z_d is taken to be h, in the second 2/3 h, which is a widely used standard in forests and other complex
332 terrain applications (~~Brutseart~~Brutsaert, 1975), and in the third 1/3 h~~ for comparison, both~~. Each z_d case is computed
333 for the four realizations of h used as before. Equation 1, (for irregular obstacles) is then applied to the roughness
334 elements remaining above the plane of the general surface slope offset by a distance z_d above the minimum height of
335 the surface mesh. The representative height h for this portion of the mesh exceeding the plane is taken to be the
336 mean area-weighted height of all triangles above this plane, s is the summed frontal area of all mesh triangles above
337 z_d that face into the chosen wind direction and S is the total horizontal area of the surface components above z_d.

338 Munro (1989, 1990) modified the formula of Lettau (1969) to be applied to a single irregular surface cross-section
339 of length X, sampled perpendicular to the wind direction. This modified formulation is easier to work with on a
340 glacier where the roughness elements are irregular, closely spaced, and generally poor approximations of objects
341 distributed over a plane. Instead of having to define an obstacle height above the plane, h is replaced with an
342 effective height $h*$ expressed as twice the standard deviation from the standardized mean profile height; s is replaced
343 with $h*X/2f$, in which f is the number of profile sections that are above the mean elevation; and S is replaced with
344 $(X/f)^2$. This approach approximates the surface elevation profile as rectangular elements of equal size, and has been
345 shown to give results within 12% of the silhouette area determined by integrating between true topographic minima
346 (Munro, 1989). Importantly, roughness values derived this way over snow, slush and ice surfaces show reasonable
347 agreement with roughness values derived from wind profiles (Brock et al., 2006). To investigate the nature of the
348 roughness computed this way for north-south and east-west impinging wind directions, cross profiles longer than
349 1.5 m at 0.~~1m~~1 m intervals orientated E-W and N-S were extracted from each scanned surface. Cross-sections were
350 detrended to remove the influence of any general surface slope at the site, and roughness was computed on each of
351 these cross-sectional profiles following the modifications of Munro ~~for each detrended surface profile~~. Mean profile
352 roughness for these two wind directions are presented for each sampled surface.

3. Results

3.1 Evaluation of the quality and suitability of penitente scans by TLS and Kinect

At the~~The~~ test site~~, the~~ was well-developed snow penitentes ~~were well developed and between~~ 0.5 ~~and~~ 1.0 m in height in a channel (Figure 1b). TLS scans ~~were made~~ of these penitentes ~~to illustrate the capabilities of this more conventional scanning system in capturing the penitente surfaces. TLS scans~~ were taken from five different vantage points ~~positioned~~ above the penitentes. The penitente surface produced by the TLS had surface slope ranging between -30 and 90 degrees, indicating that overhanging surfaces within the penitente field ~~are~~can be captured~~, however~~. However the limitations of this conventional fixed-point scanning system in capturing the penitente surfaces is illustrated by the fact that only 58% of the total surveyed horizontal area could be scanned, as the deepest parts of the troughs were obscured from the view~~ of TLS~~ by the surrounding penitentes (Figure 2a). By comparison, the hand-held, mobile nature of the Kinect means that ~~100% of~~ the whole surface of the penitente field can be captured as the field of view can be adjusted into almost limitless close-range positions. ~~The long range of the TLS makes it easier to cover large areas in comparison to~~, although the close range Kinect sensor~~, but as only penitente tips are scanned the utility of this larger areal coverage~~ is ~~limited~~impractical to apply over large areas.

~~The Kinect scan~~For the direct comparison of the two methods on a reference boulder~~,~~ the Kinect-derived surface, produced from three mosaicked meshes was aligned to ~~that~~the surface produced from the TLS point clouds. The TLS scan was incomplete, with parts of the top and overhanging surfaces of the boulder missing due to being obscured from the TLS survey positions, while the Kinect scan achieved complete coverage of the boulder. The difference between the two aligned meshes where overlapping data existed was always < 2 cm (Figure 2b), which is well within the error of the georeferenced TLS surface model. Larger differences in Figure 2b, up to 5 cm, occur only where there are holes in ~~one of~~ the surfaces being compared.

It is difficult to formally assess the total error of the surfaces produced by the Kinect scans because the ~~proprietary software, ReconstructMe™ and Poisson surface reconstruction in Meshlab, are all~~workflow involves several black box processing steps~~ in the workflow~~. The mean alignment errors of the mesh mosaicking step in Meshlab is < 0.4 cm and quantifiable errors associated with the GPS positions, subsequent measurement of the stake bottom positions relative to the GPS positions are all < 2.0 cm. However, ~~in this study~~ the three-dimensional georeferencing error in this study is large (Table 1) compared to the other sources and ~~can be~~is therefore taken as a reasonable value for the error of the total process chain. Errors given on the seasonal mass, volume and surface changes are based on summing the squares of the mean elevation difference between the marker stakes and ground control points (GPCs) at each site on the first and last survey dates.

3.2 Meteorological conditions

During the study period one significant snowfall event occurred on the 8th December 2013, when the sonic ranger recorded ~~an increase of~~ a surface height increase of 0.09 m over the course of the day~~, and temperature and incoming longwave radiation increase progressively~~ (Table 2). ~~The surface conditions of~~Surface albedo and ~~surface~~ temperature are derived from radiation measurements that ~~integrate the signal from a~~ sample an area beneath the instrument. Surface temperature was calculated from measured surface longwave emissions, assuming ~~a surface longwave~~ emissivity of 1. Over the study period, air temperature and atmospheric longwave receipts increase, while albedo decreases and derived surface temperature increases (Table 2). Thus, over the course of the study, ~~the~~ atmospheric energy supply increases and ~~the~~ surface properties become ~~gradually~~ more conducive to melting. ~~In the three measurement periods 22, 38 and 43% of hourly values of surface temperature exceed the melting point and the~~The warming atmosphere is clearly expressed in the positive degree days of the three periods which are 3.7, 2.2 and 31.5 over the 16, 9 and 14 day-long periods respectively. ~~The height change difference~~Hourly surface temperatures exceed the melting point in 22, 38 and 43% of cases in each period respectively. Daily surface lowering rates calculated between ~~the~~ hourly mean sensor-to-surface distance recorded by the AWS sonic ranger at midnight at the end of the survey days indicates lowering rates of 17, 37 and 56 mm day^{-1} over the ~~same~~three measurement intervals, ~~indicating~~confirming that the increasing energy receipts translate into increasing rates of surface lowering at the AWS.

3.3 Areal scans of penitente surfaces

Surface lowering rates derived from the ~~computed~~calculated volume changes per unit area are 21, 41 and 70 mm day^{-1} over each interval at site A, and 57 and 61 mm day^{-1} over the last two intervals at site B. Surface lowering calculated as the difference between successive hypsometric mean mesh elevation for each site were within a few millimetres of the volume computations: 22, 38 and 69 mm day^{-1} for the three measured intervals at site A, and 54 and 60 mm day^{-1} for the last two intervals at site B. The total surface lowering over the whole available period computed by volume change (hypsometric mean height change) was 1.68 (1.77) ± 0.11 m at site A and 1.37 (1.32) ± 0.38 m at site B. Surface height changes recorded at site A over the same period as at site B were 1.35 (1.31) ± 0.21 m, indicating that the values were repeatable ~~across~~at both sites. The volume loss was converted to mass loss ~~on the basis of~~using the mean snow density of 426 kg m^{-3} (with an assumed error of ± 5%) measured in a 1.10 m snow pit excavated on 22 November 2013 beside the ~~weather station.~~AWS. Mass loss at site A computed from mesh volume ~~changes~~change (hypsometric height ~~changes~~change) between 25 November and 3 January was 716 ± 58 (754 ± 59) kg m^{-2}~~, indicating an underestimation of mass loss but that the two computation methods are within error of each other~~. Mass loss at site B from mesh volume changes (hypsometric height changes) between 11 December and 3 January was 582 (562) ± 166 kg m^{-2}. Measurements at site A over the same period give mass loss of 573 (558) ± 95 kg m^{-2}, so again, measurements at both sites are within error of each other.

The morphometry of the sampled penitentes changed visibly over the measured intervals (Figures 3 and 4). The strong east-west ~~preferential orientation~~lineation and preferred north and south surface aspect predicted from theory developed early and was maintained throughout study period. ~~The expression of this alignment is more convoluted in the stages of development studied here than the parallel rows of penitentes used in model representations (Corripio and Purves, 2005; Lhermitte et al., 2014).~~ Over time ~~the~~ penitente troughs became fewer in number, but wider and deeper ~~in keeping with the increasing surface relief evident in the manual measurements.~~. This ~~is reflected by increasing~~causes total surface area~~, with the penitente surfaces~~ to increase; at site A ~~providing~~the true surface is between 1.7 and 4.0 times the ~~surface area of the~~ horizontal equivalent area, ~~and at site B providing~~ between 2.1 and 3.7 times the horizontal surface area equivalent and at site B (Figure 4 a & b). Snowfall during the first measurement interval decreases the surface area at site A over that interval. ~~The surface~~Surface relief, expressed by the vertical range of the mesh, also increases through time, except when snowfall partially filled the developing penitentes~~, reducing~~ and reduces both the range of the surface and the general slope angle. ~~Nevertheless, the morphometric~~

439 ~~properties of the meshes broadly meet the properties of simplified surfaces.~~ The largest part of the surface is facing
440 southwards, and the predominant angle generally steepens over time, though again this trend is reversed by snowfall
441 (Figure 4 c & d). From the onset of measurements the surface aspect distribution is strongly dominated by north and
442 south facing components and this becomes more pronounced in the latter measurements and the preferred
443 orientation rotates slightly over the course of the season (Figure 4 e & f).

~~3.4~~3.4 Manual measurements of reference cross-profile

445 The surface properties from manual measurements were computed on data sampled at 0.2 m over 5.0 m. Maximum
446 relief of the sampled penitente profile, defined as the range of the distance from the horizontal reference to the
447 surface, increased over time from 0.76, through 0.83 and 1.00 to 1.38 m on each measurement date. The standard
448 deviation of the surface remained relatively unchanged with values of 0.24, 0.26, 0.28 and 0.32 m at each
449 measurement date. Surface lowering rate calculated by differencing the mean surface height along the profile on
450 each measurement data was 13, 57 and 61 mm d^{-1} over the three sampled intervals, giving a total mean surface
451 lowering of 1.61 ± 0.14 m between 23 of November and 4 January. These manual measurements along the cross-
452 profile compare well to the aerially-averaged lowering rates from the scanned surfaces, despite the fact that the
453 manual measurements are made in only 2 dimensions, do not visually represent the complexity of the penitente
454 surfaces, and individual points are sometimes out of the range of error of the Kinect (Figure 5). The computed mass
455 loss over the same period is 688 ± 70 kg m^{-2}, which underestimates, but is within error of, the value for site A
456 derived from volume changes.

457 To investigate the impact of sampling resolution, maximum elevation range, mean surface height compared to the
458 horizontal reference and mean surface lowering were calculated from manual measurements at 0.1 (n = 52), 0.2 (n =
459 26), 0.4 (n = 14) and 1.0 m (n = 6) intervals on the last three measurement dates. The highest resolution sample was
460 taken as a reference against which to evaluate coarser sampling. Surface relief differed from that measured at 0.1 m
461 by maxima of 0.13, 0.29 and 0.41 m for 0.2, 0.4 and 1.0 m sampling intervals respectively. Mean measured surface
462 height was within 0.03 m of the highest resolution measurements at 0.2 m and 0.4 m intervals, and within 0.12 m at
463 1.0 m resolution. Mean lowering rates at 0.1, 0.2 and 0.4 m sampling intervals were all within 3 mm d^{-1}. This
464 increased to a maximum of 12 mm d^{-1} when the sampling resolution was decreased to 1.0 m. Decreasing the length
465 of the sampled profile down to 2 m alters the mean lowering rate by less than 5 mm ~~day~~$^{-1}$ at sampling resolutions of
466 0.1, 0.2 and 0.4 m.

467 Probing of the snow depth on 25 November indicated mean snow depth of 1.83 m (standard deviation 0.56 m). The
468 underlying ice surface does not appear to be influencing the structure of the overlying snow penitentes (Figure 5).
469 However, it is difficult to draw a firm conclusion based on these measurements, particularly as, while the surface of
470 the penitentes was still snow on the 3 January, in several instances the surface had lowered below the level of the ice
471 interface suggested by the initial probing.

3.5 Surface roughness assessments

473 Given that aerodynamic measurements to determine the most suitable representative height and zero displacement
474 level for penitentes are thus far unavailable, the approach taken here was to do an exploratory study and compute
475 geometric surface roughness values using various ways of expressing h and z_d. As a consequence the results are
476 purely illustrative and while patterns can be drawn from them that have meaning for understanding the nature of the
477 computation, the applicability of these values in turbulent exchange calculations remains to be established. The
478 representative height, h, used in the calculations increases over time in all cases, and is bounded by the maximum
479 case, taking h ~~to be the~~as range of the detrended surfaces ~~(maximum)~~, and the minimum case, taking h as twice the
480 standard deviation of the detrended surface (Figure ~~5~~6). For clarity, the ~~other~~ two ~~case~~intermediate values are not
481 included in ~~the plots shown here.~~Figure 6. Differences ~~within a single~~in h computed by the same method ~~between~~

482 ~~the two sites~~ can reach as much as 0.2 m between the two sites, although the pattern of change over time is
483 consistent.

484 The application of ~~Lettaus~~Lettau's (1969) formula is considered to be invalid if the ratio of the frontal area to the
485 planar area of the obstacles exceeds 0.2 – 0.3, with 0.25 often being chosen as a single value. ~~In~~This ratio is greater
486 than 0.2 for all ~~cases~~ of the penitente surfaces ~~this ratio exceeds 0.2, and~~ ~~only 6% of cases computed at 10° intervals~~
487 ~~of bearing over all dates are below 0.3, and these are all early in the season, before~~after the 20th December is always
488 greater than 0.3. Exceeding this threshold implies that the obstacles are so closely packed that 'skimming' airflow
489 will occur. Ignoring this issue, calculated z_0 values increase with time and show a strong dependence on the
490 impinging wind direction, with values peaking for wind directions perpendicular to the alignment of the penitentes
491 (Figure ~~6~~7). Calculated z_0 ranges from 0.01 – 0.90 m, depending on the way in which the representative height is
492 expressed, the ~~time of year~~date and the wind direction (Figure ~~7~~8). However, given the close spacing of the
493 penitentes it ~~seems appropriate~~is likely more valid to ~~also~~ explore what the calculated z_0 would be ~~like~~ when
494 ~~applying~~ a zero displacement height offset~~, although again~~ is applied. Again, in the absence of validation data ~~these~~
495 ~~numbers~~from independent measurements, calculated values can be only indicative of the pattern of roughness
496 computed by these methods. Introducing the zero displacement height reduces the maximum calculated roughness
497 by about half, and also reduces the variability between different representative heights (Figure ~~7~~8), as a smaller h
498 value translates into a smaller z_d so that the calculation is performed on a larger portion of the mesh.

499 Surface roughness assessments on the basis of calculations following Munro's modification for single profile
500 measurements were applied to cross profiles longer than 1.5 m yielding 20 (6) profiles orientated N-S and 33 (7) E-
501 W at site A (B). Surface amplitude increases over time, and the amplitude of the N-S running cross profiles is
502 generally larger than the E-W running cross profiles, as illustrated in the example of site B (Figure ~~8). The~~9). Table
503 3 shows the calculated roughness values at each survey date, revealing that while profile-computed roughness
504 length increases monotonically over time at site B, ~~but shows a reduction~~it reduces over the first period at site A,
505 associated with snowfall during this period. Both the range and relative increase in roughness over time is larger for
506 the N-S running profiles. The computed roughness at both sites is 4.3 to 6.8 times larger for airflow impinging on
507 the penitente field in an E-W direction than for airflow in the N-S direction. This is contrary to the results computed
508 on the full 3D mesh surface, but is understandable because this formulation relies on the amplitude of the surface,
509 which is generally larger in the N-S orientated cross profiles than the E-W running cross profiles.

510 **4. Discussion**

511 **4.1 Penitente morphology**

512 Although the natural penitentes sampled here are more convoluted than the parallel rows of penitentes used in model
513 representations (Corripio and Purves, 2005; Lhermitte et al., 2014), the morphometric properties of the meshes
514 broadly meet the properties of simplified surfaces. The penitente surface represents a much larger total surface area
515 than the equivalent non-penitente surface and the control of solar radiation on penitente morphology means that the
516 vast majority of the surface consistently dips steeply to the north and south at all stages of development. This means
517 that the angle of incidence of direct solar radiation is reduced, decreasing both the intensity of the solar beam and the
518 proportion of it that is absorbed. Although these effects are counteracted by multiple reflections of solar radiation
519 within the penitente (Corripio and Purves, 2005; Lhermitte et al., 2014; Claudin et al., 2015) modeled mean net
520 shortwave at sampled points in an example penitente field at the summer solstice at 33°S is about half of that of a
521 level surface (Corripio and Purves, 2005). However, given the larger surface area of the penitente field compared to
522 a flat surface, the total absorbed shortwave is a third higher in the modeled penitentes, broadly in line with the
523 observed effect of penitentes on spatially-averaged albedo (Warren et al, 1998; Corripio and Purves, 2005;
524 MacDonell et al., 2013; Cathles et al., 2014; Lhermitte et al., 2014). For idealized penitentes at 33°S during summer
525 solstice, modeled increase in net shortwave radiation over penitentes is not compensated by modelled changes in net

longwave radiation, meaning that the excess energy receipts must be compensated by either turbulent energy fluxes or consumption of energy by melting (Corripio and Purves, 2005).

Unless a snowfall event occurs to partially fill the troughs, surface relief, slope angle, penitente spacing and total surface area all increase over time as the penitentes develop and deepen. Thus the impact of penitentes on surface properties will also change along with the morphological changes. At Tapado Glacier, penitentes are initially overhanging to the north, and the southfacing sides are convex compared to the northfacing overhanging faces. Over the season the penitentes become more upright as the noon solar angle gets higher. Idealized modelling based on measurements at Tapado Glacier, shows that concave and convex slopes, as well as penitente size have been shown to impact the apparent albedo as measured by ground and satellite sensors (Lhermitte, et el., 2014), and there may be some value in assessing the impact of these morphometry changes on albedo over time. In the context of the numerical theory of Claudin and others (2015), penitente spacing controls the atmospheric level at which water vapor content is representative of the bulk surface properties. Simultaneous field or laboratory measurements of penitente spacing evolution and vapor fluxes above the surface would be required to solidly confirm this, but the spacing from the field measurements provided here can be used as an indication of the level at which measurements would need to be made in order to capture the bulk surface fluxes rather than fluctuations governed by the small-scale surface terrain.

4.2 Prevailing wind direction differs only slightly in each period with an increasing northwesterly component in the second two periods compared to the first. This may be related to the occurrence of snow during the first period, which can be expected to alter the thermally driven valley wind systems. Over the whole study period wind direction is predominantly from the south westerly sector, but swings through southerly to easterly thereby encompassing both extreme wind angles used in the roughness calculations here (Figure 9). This indicates that the effective roughness can be expected to differ significantly depending on the wind direction.

3.5 Manual measurements of reference cross-profile

Using data sampled at 0.2 m over 5.0 m, the maximum relief of the sampled penitente profile, defined as the range of the maximum and minimum distance from the horizontal reference to the surface, increased through time, from 0.76, 0.83, 1.00 to 1.38 m on each measurement date. The standard deviation of the surface remained relatively unchanged over time with values of 0.24, 0.26, 0.28 and 0.32 m at each measurement date. The difference in the mean surface height measured at the ablation frame profile at site A indicates mean lowering rates of 13, 57 and 61 mm day^{-1} over the three sampled intervals resulting in a total mean surface lowering of 1.61 ± 0.14 m between 23 of November and 4 January. The manual measurements at the cross profile compare well to the aerially averaged lowering rates from the scanned surfaces, despite the fact that the manual measurements are only made in 2 dimensions, do not visually represent the complexity of the penitente surfaces, and individual points are sometimes out of the range of error of the Kinect (Figure 10). The computed mass loss over the same period is 688 ± 70 kg m^{-2}, which underestimates the value for site A derived from volume changes but is within error, even accounting for the two extra days measurement interval.

Values of maximum elevation range and standard deviation along the profile, mean surface height compared to the horizontal reference and mean lowering were computed from the manual measurements for available data at 0.1 (n = 52), 0.2 (n = 26), 0.4 (n = 14) and 1.0 m (n = 6) intervals to investigate the impact of sampling resolution. The highest resolution sample was taken as a reference against which to evaluate the values from coarser resolution sampling. Calculated surface relief differed from that measured at the highest resolution by maxima of 0.13, 0.29 and 0.41 m for 0.2, 0.4 and 1.0 m sampling intervals respectively. Mean measured surface height was within 0.03 m of the highest resolution measurements at 0.2 m and 0.4 m intervals, and within 0.12 m at 1.0 m resolution. Mean lowering rates at 0.1, 0.2 and 0.4 m sampling intervals were all within 3 mm day^{-1} with the difference increasing to a maximum of 12 mm day^{-1} when the sampling resolution was decreased to 1.0 m. Decreasing the length of the

578 **4. Discussion**

579 **4.1 Methods of measuring change of rough glacier surface elements**

580 The test site for scanning penitentes with a TLS was chosen as it provided the most optimal viewing angles possible
581 from scanning positions, as the penitentes lay in a river bed and scanning positions could be established on the
582 surrounding river banks to look down intohigher ground overlooking the penitente field., thereby offering the best
583 viewing angles possible. Nevertheless, the terrestrial laser scanning could only capture the tips rather than the whole
584 surfaceupper portions of the penitentes and, as. As ablation is at its maximum in the troughs, TLS data is therefore
585 not able to determine the true volume change ongoing inof penitentes. The coverage would be increased if a higher
586 viewing angle could be achieved, but the steep, dense nature of penitente fields makes it difficult to imagine where
587 sufficient suitable locations can be found surrounding glaciers or snowfields with penitentes. In contrast, the mobile
588 Kinect sensor can be moved across the complex relief of the penitente field to make a complete surface model.
589 Although it is in principle possible to capture a large area with the ReconstructMe software used here, and it offers
590 the advantage of providing real time feedback on the mesh coverage, it proved difficult to capture the study sites in a
591 single scan given (i) the reduced signal range of the sensor over snow and ice (Mankoff et al.,and Russo, 2013), and
592 (ii) the difficulty of moving around the penitente field. As a result, partial scans were obtained, with the
593 disadvantage that subsequently combining these introduces a substantial degree of additional error associated with
594 alignment if the component scans were not of high quality at the margins, or did not overlap adjacent scan areas
595 sufficiently. A combination of these two techniques might allow the extrapolation of small-scale geometry changes
596 and volume loss determined from a Kinect surface scan to be extrapolated usefully to the glacier or snowfield scale
597 using measurements made with a TLS.

598 Despite not visually capturing the complex surface propertiesmorphology of the penitentes, manual measurements
599 of surface height change in a penitente field along a profile cross-cutting the penitentes are robust for determining
600 mean surface lowering rates, and show good agreement to the volume changes computed from differencing the
601 digital surface models scanned in detail using a Kinect. Thus, the detailed surface geometry need not be known in
602 order to reasonably calculate the total volume loss over time within penitente fields. Comparison of the manual
603 sampling at different intervals suggestsuggests that five samples per meter is adequate to characterize surface change
604 of penitentes., but that data will be unreliable is the cross-profile is too short. Over the 39 days of the study, the mass
605 loss calculated from 26 points spaced at 0.2 m intervals along a 5 m profile crosscutting the penitentes differed from
606 that calculated from volume change computed on surface meshes consisting of over 1.3 million points and covering
607 an area of 7 m^2 by only 28 kg m^{-2}. Although this difference was within the error of the two measurement types, the
608 seasonal difference, assuming that this difference applies to a whole ablation season of 120 days would be 86 kg m^{-2},
609 and applied to the whole glacier (3.6 km^2) would amount to an underestimate of mass loss over an ablation season of
610 0.3 gigatonnes. As a side note, the probing of snowdepth carried out as part of this study highlights the difficulty in
611 identifying the underlying ice surface, or summer ablation surface, in this way within a penitente field, suggesting
612 that a single location must be sampled very densely to obtain a characteristic snowdepth inby this waymethod.

14

4.3 Surface roughness

~~4.2 Penitente~~The changing morphometry ~~and change in time~~

~~The manual measurements at 0.2 m intervals are adequate to determine the mean surface lowering within a penitente field, giving confidence to this type of simplified measurement on seasonal timescales. However, the interval measurements cannot capture the surface morphometry, or how it changes in time.~~

~~At all times the penitente surface represents a much larger total surface area than the equivalent non penitente surface. Over time the surface relief, and slope angle, increases as~~ the penitentes ~~deepen, unless a snowfall event occurs to partially fill the troughs, which also reduced the mean surface slope. The control of solar radiation on penitente morphology means that the vast majority of the surface consistently dips steeply to the north and south at all stages of development. This means that the angle of incidence of direct solar radiation is reduced, decreasing both the intensity of the solar beam and the proportion of it that is absorbed. Although these effects are counteracted by multiple reflections of solar radiation within the penitente (Corripio and Purves, 2005; Lhermitte et al., 2014; Claudin et al., 2015) modeled mean net shortwave in an example penitente field at the summer solstice at 33°S is about half of that of a level surface (Corripio and Purves, 2005). However, given the larger surface area of the penitente field compared to a flat surface, the total absorbed shortwave is a third higher in the modeled penitentes. At Tapado Glacier, penitentes are initially overhanging to the north, and the southfacing sides are convex compared to the northfacing overhanging faces. Over the season the penitentes become more upright as the noon solar angle gets higher. Idealized modelling based on measurements at Tapado Glacier, shows that concave and convex slopes, as well as penitente size have been shown to impact the apparent albedo as measured by ground and satellite sensors (Lhermitte, et al., 2014), and there may be some value in assessing the impact of these morphometry changes on albedo over time. For the idealized penitente surface at 33°S during summer solstice case, modeled increase in net shortwave radiation over penitentes is not compensated by modelled changes in net longwave radiation, meaning that the excess energy receipts must be compensated by either turbulent energy fluxes or consumption of energy by melting (Corripio and Purves, 2005).~~

~~In the context of the numerical theory of Claudin and others (2015), progressive widening of the penitente spacing, as observed at both site A and B, is indicative of changes in the atmospheric level at which water vapor content is unaffected by the vapor flux from the penitente surface. Simultaneous field or laboratory measurements of penitente spacing evolution and vapor fluxes above the surface would be required to solidly confirm this, but the field measurements provided here can be used as an indication of the level to which vapor flux from the surface is influencing the boundary layer vapor content.~~

alters the geometrical surface roughness as they develop over the ablation season. Values calculated using~~4.3 Surface roughness~~

~~In this work~~ a single, simple, geometric relationship (Lettau 1969) ~~was~~were investigated because a profile-based version of this formulation has previously been tested against aerodynamic measurements over glacier surfaces (Munro, 1989, 1990; Brock et al., 2006). Certainly other relationships could be explored in the context of linearized glacier features, but given the wide spread of values produced in previous comparisons such an analysis might be of limited value in the absence of simultaneous aerodynamical investigations (Grimmond and Oke, 1999). Furthermore, the results of Grimmond and Oke (1999) indicate that for the cities sampled, the Lettau method gives z_0 values that are in the middle of the range of all the methods. The analysis of geometric computations of roughness properties in Grimmond and Oke (1999) highlight the importance of correctly determining z_d, and limited sensitivity analyses show the computed z_d and z_0 to be strongly dependent on the dimensions of the obstacles. Lettau's (1969) formula, which does not account for z_d, overestimates roughness for densely packed obstacles, but this ~~overestimation~~ does not compensate sufficiently to reproduce values of $z_d + z_0$ ~~produced~~ for densely packed obstacles from formulations that include z_d in the computation of z_0. ~~This means that~~Thus, Lettaus formula is

expected to estimate the zero velocity point of a logarithmic wind profile to be lower than formulations that include z_d in ~~their computation of z_0. In this work however we computed z_d in a separate preceding step to explore the impact of z_d on the computed~~the computation of z_0.

~~As penitentes fields present very densely packed roughness elements, the frontal area of the surface tends to be large compared to the ground area, and the limits of the~~ The ratio of frontal to planar area ~~found in this study~~ of the penitentes implies that skimming flow ~~is almost always occurring over penitente fields~~prevails, such that turbulent airflow in the overlying atmosphere does not penetrate ~~to the full depth of the~~penitente ~~fields~~troughs. This is in agreement with the theory of formation and growth of penitentes~~,~~ in which the development and preservation of a humid microclimate within the penitente ~~hollows~~troughs is required to facilitate differential ablation between the trough and tip of the penitente. ~~As~~Although the ~~spacing between the~~data here shows that penitentes ~~also increases over the ablation season the features~~become less densely packed over time, ~~although the~~skimming flow regime persists over the study period, and available data ~~are~~is insufficient to determine if ~~the spacing increases sufficiently by the~~this holds true to the end of the ~~season to comply with the applicable limits of the roughness calculation used here~~ablation season.

Application of geometrical roughness equations is made more problematic in penitente fields as it is not clear how an appropriate representative obstacle height should be expressed, nor how to define the zero displacement level during ~~presumed~~ skimming flow. Roughness calculated using a range of possible representations of these properties point towards roughness values in the order of 0.01-0.10 m during the early part of the ablation season and 0.10-0.50 m after the end of December. These values are in line with the roughest values previously published for glacier ice (Smeets et al., 1999; Obleitner, 2000). The topographic analysis clearly shows that in the absence of intervening snowfall events, this roughness increase is related to the deepening of the penitentes over time and an increase of the surface amplitude. The ~~patterns~~pattern of the computed roughness properties is consistent between the two neighbouring sites, but individual values can differ, suggesting that ~~local~~relief varies substantially over short distances and sampling a ~~larger~~large area ~~would be beneficial in order~~is necessary to capture mean properties.

The strong alignment of penitentes means that ~~roughness~~calculated roughness is strongly dependent on ~~the~~wind direction. Roughness calculated from 3D surface meshes ~~is~~are higher for wind impinging in a north-south direction, as the large faces of the penitentes form the frontal area in this case. In contrast, ~~if~~roughness ~~is computed~~calculated for individual profiles extracted from the mesh to mimic manual transect measurements in the field, ~~roughness~~is between 3 and 6 times larger for air flow ~~along the penitente lineation (E-W) than it is across the lineation (N-S). While clearly highlighting that the surface roughness of the strongly aligned penitente fields is dependent on wind~~impinging in an east-west direction, ~~this contradiction poses~~than in a ~~conundrum as neither~~north-south direction. Neither approach has been ~~specifically~~ evaluated against independent surface roughness derived from atmospheric profile measurements over penitentes. Consequently, although surface roughness calculations on the basis of profile geometry have been evaluated against aerodynamic roughness over rough ice surfaces, the available data is insufficient to distinguish if maximum aerodynamic roughness is associated with wind flowing across or along the penitente lineation. Thus it is not clear which ~~pattern is more~~method captures the appropriate relationship between wind direction and surface roughness for calculating turbulent fluxes over penitentes. It principle it sounds reasonable to expect airflow across the penitente lineation to maximize turbulence as the penitentes present a large surface area to the wind, yet, if skimming flow is established, with the result that only the tips of the penitentes are determining the structure of the turbulence then roughness in this direction would be strongly reduced, and perhaps even be less than for air flow along the penitente lineation, for which the smaller frontal area reduces the likelihood of skimming flow. Further investigation of this in order to quantify the impact of penitentes on turbulent fluxes for various airflow patterns requires measurement of turbulent fluxes using eddy covariance or atmospheric profile methods, which would demonstrate the nature of the directional roughness and establish the impact of penitentes on turbulent energy fluxes for different wind directions. Such measurements would be best implemented in a manner which can sample all wind directions equally, and eddy covariance systems for which analysis is limited to a sector

703 of airflow centred around the prevailing airflow source, might not be able to capture the nature of the directional
704 dependence correctly.

705 Prevailing wind direction differs only slightly in each period with an increasing northwesterly component in the
706 second two periods compared to the first. This may be related to the occurrence of snow during the first period,
707 which is expected to alter thermally-driven valley wind systems. Over the whole study period wind direction is
708 predominantly from the south-easterly and north-westerly sectors, and swings through both extreme wind angles
709 used in the roughness calculations here (Figure 10). This indicates that the effective roughness at this site can be
710 expected to differ significantly over time depending on the wind direction.

711 In this study we did not explicitly compute the blending height as available formulae are dependent upon z_0 and z_d.
712 Estimates of the blending height independently from z_0 and z_d have been suggested to be 2.5 - 4.5 times h, as twice
713 the mean element spacing, or as combination of the height and spacing (see examples within Grimmond and Oke,
714 1999). Given that only atmospheric measurements above the blending height give representations of integrated
715 surface fluxes and conditions, the first approach would imply that aerodynamical or flux measurements over
716 penitentes would have to be carried out at ~~some~~considerable height above the surface to capture mean surface
717 properties rather than the effects of individual roughness elements. The mathematical model of Claudin and others
718 (2015) ~~indicates that the~~ gives a characteristic length scale for the level at which the vapour flux ~~does not~~ is constant
719 in horizontal space~~, and therefore is the product of mean surface properties,~~ that is related to the spacing of the
720 penitentes. ~~Taking~~Interpreting this ~~to be representative of~~level as the blending height ~~would imply~~implies that ~~a~~
721 ~~formulation for~~ the blending height might be ~~possible~~determined on the basis of spacing of penitentes alone, and that
722 this in turn might contain useful data for understanding the structure and efficiency of turbulence above penitentes.
723 ~~However, exploring~~Exploring these ideas requires information from detailed meteorological measurements as well
724 as the geometrical information offered in this paper.

725 **5. Conclusion**

726 Surface scanning technology and software is an area of rapid development, and a number of potentially superior
727 alternative set-ups and data capture sensors and software is now available. This study demonstrates that the
728 Microsoft Kinect sensor can work successfully at close range over rough snow and ice surfaces under low light
729 conditions, and generate useful data for assessing the geometry of complex terrain and surface roughness properties.

730 The data collected offers the first detailed study of how the geometry of penitentes ~~evolves~~evolve through time,
731 highlighting the rate of change of surface properties over an ablation season that can serve as a guideline for
732 parameterizing surface properties required for energy and mass balance modelling of penitente surfaces.

733 The ~~measurements~~results confirm that even relatively crude manual measurements of penitente surface lowering are
734 adequate for quantifying the seasonal mass loss, which is good news for the validity of measurements of surface
735 change on glaciers with penitentes. However, further measurements and/or modelling studies are required to
736 determine if the mass loss from the expanded and convoluted surface of penitentes is enhanced or inhibited
737 compared to mass loss in the absence of penitentes.

738 Aerodynamical roughness properties and related metrics over very rough surfaces remain poorly quantified and both
739 geometric and meteorological determinations of these values show a wide spread; consequently it remains unclear
740 what the best methods to use are or what values modellers would be best to use (Grimmond and Oke, 1999). In this
741 context ~~penitentes and~~ further study of ~~them~~penitentes offers a useful opportunity as (a) their morphometric
742 evolution over time allows various geometries to be evaluated by ~~instrumenting and scanning~~monitoring a single
743 site, and (b) they offer a bridge between wind tunnel and urban field experimentation of turbulence and roughness
744 over extreme terrain. Although validity of surface roughness calculations based on surface geometry remains to be

established for penitentes, this study highlights that (i) skimming flow is expected to persist over penitentes field, but is more likely under wind directions perpendicular to the penitente alignment; (ii) z_d is certainly greater than zero, and while the depth of penetration of surface layer turbulence into a penitente field is not clearly established it is likely to evolve with the developing penitentes, and values of $z_d \sim 2/3h$ give results that are theoretically reasonable in the framework outlined by Grimmond and Oke (1999); (iii) the two methods of geometric computation of surface roughness applied here give conflicting results as to whether the effective surface roughness of penitentes is greater for airflow along or across the penitente lineation and (iv) more complete understanding of the impact of penitentes on the turbulent structure, its evolution in time, and its directional dependency, would require atmospheric measurements with no directional bias concurrent with measurements of penitentes morphology.

Potential future applications and analyses of the surfaces generated in this study include (i) using surface properties and roughness values as a guide for input into surface energy balance models; (ii) assessing the performance of models against the measured volume loss over time and (iii) evaluating how well simplified representations of penitente surfaces used in small scale radiation models and turbulence models capture the real-world complexity. Such studies would help establish the nature of the likely micro-climatic distribution of the surface energy balance within a real penitente field, and as a result the impact of penitentes on runoff and exchange of water vapour with the atmosphere.

References

Amstutz, G. C. (1958) On the formation of snow penitentes. *Journal of Glaciology*, 3 (24), 304-311.

Andreas, E. L. (2011). A relationship between the aerodynamic and physical roughness of winter sea ice. *Quarterly Journal of the Royal Meteorological Society*, *137*(659), 1581–1588. doi:10.1002/qj.842

Bergeron, V., Berger, C., & Betterton, M. D. (2006). Controlled irradiative formation of penitentes. *Physical Review Letters*, 96(9), 098502, doi:10.1103/PhysRevLett.96.098502

Blumberg, D., & Greeley, R. (1993). Field studies of aerodynamic roughness length. *Journal of Arid Environments*. 25(1), 39-48. doi:10.1006/jare.1993.1041

Brock, B. W., Willis, I. C., & Sharp, M. J. (2006). Measurement and parameterization of aerodynamic roughness length variations at Haut Glacier d'Arolla, Switzerland. *Journal of Glaciology*, 52(177), 281–297. doi:10.3189/172756506781828746

Brutsaert, W. (1975). A theory for local evaporation (or heat transfer) from rough and smooth surfaces at ground level. *Water Resources Research*, 11(4), 543–550.

784 Cathles, L. M., Abbot, D. S., & MacAyeal, D. R. (2014). Intra-surface radiative transfer limits the geographic extent
785 of snow penitents on horizontal snowfields. *Journal of Glaciology*, 60(219), 147–154. doi:10.3189/2014JoG13J124

786 Claudin, P., Jarry, H., Vignoles, G., Plapp, M., & Andreotti, B. (2015). Physical processes causing the formation of
787 penitentes. *Physical Review E*, 92(3), 033015. doi:10.1103/PhysRevE.92.033015

788 Corripio, J. G., & Purves, R. S. (2005). Surface energy balance of high altitude glaciers in the Central Andes: the
789 effect of snow penitentes. In: De Jong C., Collins D.N. and Ranzi, R. (Eds) Climate and Hydrology in Mountain
790 Areas. Wiley and Sons, Chichester, 15-27.Drewry, D. J. (1970). Snow penitents. *Weather*, 25(12), 556.

791 Drewry, D. J. (1970). Snow penitents. *Weather, 25*(12), 556.

792 Fassnacht, S. R., Oprea, I., Borlekse, G., & Kamin, D. (2014). Comparing Snowpack Surface Roughness Metrics
793 with a Geometric-based Roughness Length. In Proceedings of the AGU *Hydrology Days 2014* Conference (pp. 44–
794 52).

795 Fassnacht, S. R., Stednick, J. D., Deems, J. S., & Corrao, M. V. (2009a). Metrics for assessing snow surface
796 roughness from Digital imagery. *Water Resources Research*, 45, W00D31 doi:10.1029/2008WR006986

797 Fassnacht, S. R., Williams, M. W., & Corrao, M. V. (2009b). Changes in the surface roughness of snow from
798 millimetre to metre scales. *Ecological Complexity*, 6(3), 221–229. doi:10.1016/j.ecocom.2009.05.003

799 Grimmond, C. S. B., & Oke, T. R. (1999). Aerodynamic Properties of Urban Areas Derived from Analysis of
800 Surface Form. *Journal of Applied Meteorology*, 38(9), 1262–1292.

801 Hastenrath, S., & Koci, B. (1981). Micro-morphology of the snow surface at the Quelccaya ice cap, Peru. *Journal of
802 Glaciology*, 27(97), 423–428.

803 Jackson, B. S., & Carroll, J. J. (1978). Aerodynamic roughness as a function of wind direction over asymmetric
804 surface elements. *Boundary-Layer Meteorology*, *14*(3), 323–330. doi:10.1007/BF00121042

805 Kaser, G., Großhauser, M., & Marzeion, B. (2010). Contribution potential of glaciers to water availability in
806 different climate regimes. *Proceedings of the National Academy of Sciences*, 107(47), 20223–20227.
807 doi:10.1073/pnas.1008162107

808 Kondo, J., & Yamazawa, H. (1986). Aerodynamic roughness over an inhomogeneous ground surface. *Boundary-
809 Layer Meteorology*, *35*(1983), 331–348.

810 Lettau, H. (1969). Note on Aerodynamic Roughness-Parameter Estimation on the Basis of Roughness-Element
811 Description. *Journal of Applied Meteorology*, 8(5), 828-832.

812 Lhermitte, S., Abermann, J., & Kinnard, C. (2014). Albedo over rough snow and ice surfaces. *The Cryosphere*, 8(3),
813 1069–1086. doi:10.5194/tc-8-1069-2014

814 Lliboutry, L. (1954). The origin of penitents. *Journal of Glaciology*, 2, 331–338.

815 Lliboutry, L. (1998). Glaciers of Chile and Argentina. In, R. S. Williams and J. G. Ferrigno (Ed). Satellite image
816 atlas of glaciers of the world: South America. USGS Professional Paper 1386-I.

817 Macdonald, R. W., Griffiths, R. F. F., & Hall, D. J. J. (1998). An improved method for the estimation of surface
818 roughness of obstacle arrays. *Atmospheric Environment*, 32(11), 1857–1864. doi:10.1016/S1352-2310(97)00403-2

819 MacDonell, S., Kinnard, C., Mölg, T., Nicholson, L. I., & Abermann, J. (2013). Meteorological drivers of ablation
820 processes on a cold glacier in the semi-arid Andes of Chile. *The Cryosphere*, 7(5), 1513–1526. doi:10.5194/tc-7-
821 1513-2013

822 Mankoff, K. D., & Russo, T. A. (2013). The Kinect: a low-cost, high-resolution, short-range 3D camera. *Earth
823 Surface Processes and Landforms*, 38(9), 926–936. doi:10.1002/esp.3332

824 Manninen, T., Anttila, K., Karjalainen, T., & Lahtinen, P. (2012). Automatic snow surface roughness estimation
825 using digital photos. *Journal of Glaciology*, 58(211), 993–1007. doi:10.3189/2012JoG11J144

826 Munro, D. S. (1989). Surface roughness and bulk heat transfer on a glacier: comparison to eddy correlation. *Journal
827 of Glaciology*, 35(121), 343–348.

828 Munro, D. S. (1990). Comparison of Melt Energy Computations and Ablatometer Measurements on Melting Ice and
829 Snow. *Arctic, Antarctic, and Alpine Research*, 22(2), 153–162. doi:10.2307/1551300

830 Naruse, R. and Leiva, J. C. (1997) Preliminary study on the shape of snow penitentes at Piloto Glacier, the central
831 Andes. *Bulletin of Glacier Research*, 15, 99-104.

832 Obleitner, F. (2000). The energy budget of snow and ice at ~~Breidamerhurjökull~~Breidamerkurjökull, Vatnajökull,
833 Iceland. *Boundary-Layer Meteorology*, 97(3), 385–410.

834 Sinclair, K. & MacDonell, S. (2015) Seasonal evolution of penitente geochemistry at Tapado Glacier, northern
835 Chile. *Hydrological Processes*, doi: 10.1002/hyp.10531.

836 Smeets, C. J. P. P., Duynkerke, P., & Vugts, H. (1999). Observed wind profiles and turbulence fluxes over an ice
837 surface with changing surface roughness. *Boundary-Layer Meteorology*, 92(1), 99–121.

838 Thomsen, L., Stolte, J., Baartman, J., & Starkloff, T. (2014). Soil roughness : comparing old and new methods and
839 application in a soil erosion model, *Soil*, 1, 399-410. doi:10.5194/soil-1-399-2015

840 Warren, S. G., Brandt, R. E., & O'Rawe Hinton, P. (1998). Effect of surface roughness ~~of~~on bidirectional
841 reflectance of Antarctic snow. *Journal of Geophysical Research*, 103(E11), 25789–25807.

842 Winkler, M., Juen, I., Mölg, T., Wagnon, P., Gomez, J., & Kaser, G. (2009). Measured and modelled sublimation on
843 the tropical Glaciar Artesonraju, Peru. *The Cryosphere*, 3(1), 21–30.

844 **Supplementary material**

845 • A: GPS position of ground control points at each glacier site
846 • B: Mesh surface components and processing steps used for Kinect surface scans
847 • C: Kinect surface meshes for both sites on all dates as .PLY files [sX_DDMM.PLY]
848 • D: 3D viewer files of surfaces at site B can be seen at:
849 https://sketchfab.com/LindseyNicholson/folders/penitentes-on-glaciar-tapado-chile

Table 1: Maximum absolute georeferencing error at each marker stake for site A and B, relative to the standard deviation of the differential GPS measurement.

	ΔX [mm]	ΔY [mm]	ΔZ [mm]	ΔXY [mm]	ΔXYZ [mm]	*dGPS XYZ standard deviation* [mm]
A-1	63	25	38	68	77	*17*
A-2	214	118	259	233	312	*15*
A-3	14	57	53	57	62	*14*
A-4	23	29	61	33	69	*16*
A-5	54	32	128	56	139	*18*
B-1	59	46	19	75	77	*16*
B-2	121	11	102	164	193	*17*
B-3	11	48	2	49	49	*12*
B-4	85	37	34	85	92	*12*

Table 2: Mean meteorological conditions during the measurement intervals: incoming shortwave (SW in), albedo (α), incoming longwave (LW in), windspeed (u), wind direction (dir), surface temperature computed from measured outgoing longwave radiation (T surface), air temperature (T air), relative humidity (RH), air pressure (P) and the distance between the sonic ranger and the glacier surface (dist).

	SW in	α	LW in	u	dir	T surface	T air	RH	P	dist
	[W m^{-2}]	[-]	[W m^{-2}]	[m s^{-1}]	[°]	[°C]	[°C]	[%]	[hPa]	[m]
sensor	*Kipp and Zonen CNR1*			*Young 05103*		CNR1	*Vaisala HMP45*		*Setra 278*	*SR50*
26/12 - 11/12	413	0.54	205	3.0	170	-5.3	-2.7	32.5	442	1.62
12/12 - 20/12	441	0.48	212	2.8	214	-2.9	-0.8	41.4	448	1.96
21/12 - 03/01	426	0.41	224	3.1	217	-1.4	1.9	39.5	456	2.56

Table 3: Surface roughness (z0) computed according to Munro (1989) on detrended profiles longer than 1.5 m, extracted at 0.10 m intervals from the Kinect surface meshes at site A and B for E-W impinging wind and N-S impinging wind. The number of profiles used for each wind direction is given in parenthesis. The likely displacement of the zero velocity plane (d_top ± standard deviation), was computed as the mean of 2/3h for all profiles and expressed as a distance from the top of the penitentes. The range of the detrended 3D mesh (3D range) provides a reference for the penetration depth of turbulence.

	site A						site B					
	z0 E-W (20)			z0 N-S (33)			z0 E-W (6)			z0 N-S (7)		
	mean	max	min	mean	max	min	mean	max	min	mean	max	min
25-Nov	45	111	11	8	19	3						
11-Dec	33	68	12	6	13	2	28	41	22	6	9	1
20-Dec	70	146	57	25	67	7	122	156	84	22	47	14
03-Jan	136	211	71	45	136	11	133	186	101	21	30	12
	3D range [m]	d_top +/- std [m]		3D range [m]	d_top +/- std [m]		3D range [m]	d_top +/- std [m]		3D range [m]	d_top +/- std [m]	
25-Nov	0.41	0.27	0.06	0.41	0.34	0.02						
11-Dec	0.48	0.33	0.05	0.48	0.41	0.01	0.58	0.45	0.02	0.58	0.51	0.02
20-Dec	0.76	0.58	0.03	0.76	0.61	0.04	0.98	0.76	0.02	0.98	0.84	0.04
03-Jan	1.07	0.79	0.03	1.07	0.86	0.05	1.14	0.86	0.03	1.14	0.98	0.02

Figure 1: Map of Tapado Glacier in the Elqui catchment of the Coquimbo Region of Chile, showing the location of the measured sites and insets of (a) the glacier site layout, showing the location of the horizontal reference (black line) and ~~:~~ (b) the test site. ~~highlighting~~ indicating the boulder ~~(*)~~ (red star) at which the Kinect scans were compared against TLS~~, and (c) an example photograph of glacier site B at the time of installation.~~.

Figure 2: (a) Oblique view of the TLS ~~-~~ derived DSM of the test site highlights the patchy coverage of the penitentes obtained by this method. (b) Absolute differences between DSMs of the sample boulder produced using TLS and Kinect.

Figure 3: Shaded DSM meshes of N-S orientated DSMs for the 1.5m x 1.5m ~~subsample at~~ glacier site B on (a) 12.12.2013 (b) 20.12.2013 and (c) 03.01.2013 obtained using the Kinect.

Figure 4: Summary of the DSM properties through time at site A (left) and B (right). (a,b) Surface height distribution as a percentage of total surface area, in local coordinates [m] relative to the position of the northern end of ablation frame ~~(a & b).~~ Inset tables show weighted mean mesh elevation, range, surface area and surface area as a function of the horizontal area of the sampled site. (c,d) Distribution of surface angles as a percentage of total surface area ~~(c & d).~~ (e,f) Aspect distribution as a percentage of total surface area ~~(e & f).~~.

Figure 5: Comparison of surface height through time extracted from the Kinect scan and measured manually along the horizontal reference. Vertical error on the Kinect cross profiles is given by a linear interpolation of total positional error between the bounding stakes. Solid black triangles indicate locations where snowdepth exceeded the length of the 3 m probe.

Figure ~~5~~6: Representative surface heights computed on detrended surface meshes for site A (solid) and site B (open) over time where h1-h4 refer to representative surface heights computed as range (h1), twice the standard deviation (h2), area weighted mean height above the minimum (h3), and area weighted median above the minimum mesh height (h4).
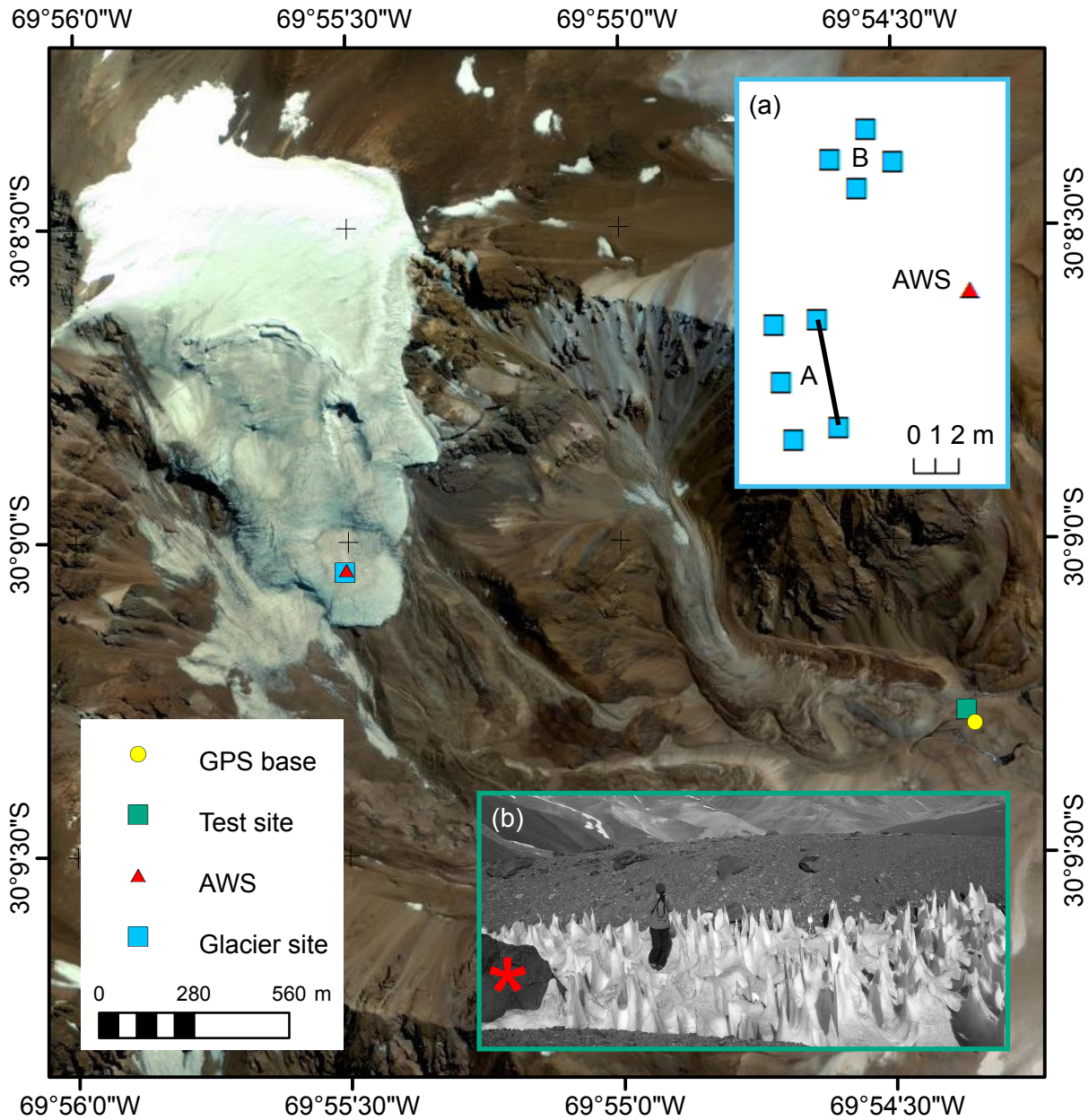
Figure ~~6~~7: 3D z_0 computed for 10° aspect intervals for all detrended DSMs highlighting peak roughness occurs in N-S airflow. Maximum values take h to be the detrended mesh elevation range, and minimum values take h to be twice the standard deviation of the detrended mesh.
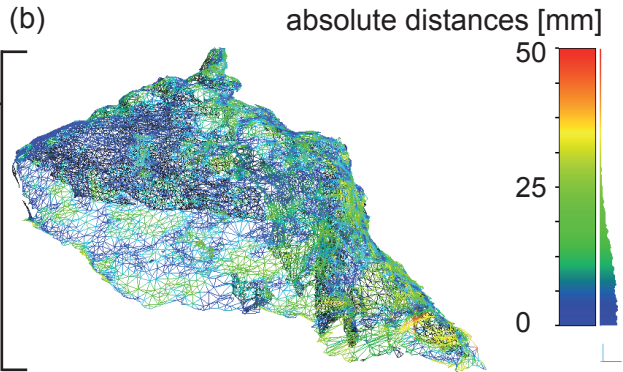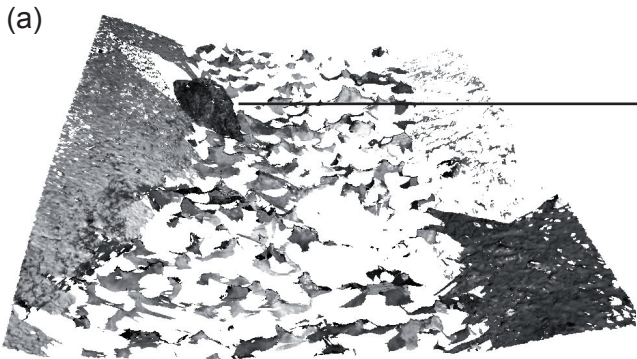
Figure ~~7~~8: Comparison of three-dimensional surface roughness through time, indicating the range of z_0 computed for all incident wind angles (at 10° intervals). Upper panels show the roughness with no zero level displacement and lower panels show values with a zero displacement offset d1 = h; d1 = 2/3h and d3 = 1/3h.As before, h1- h4 refer to representative surface heights computed as range, twice the standard deviation, area weighted mean height above the minimum, and area weighted median above the minimum mesh height respectively.

Figure ~~8~~9: Examples of (a) N-S, and (b) E-W orientated cross sections longer than 1.5 m, sampled at 0.1 m intervals ~~in local coordinates at site B~~ from which effective surface roughness properties were computed using the methods of Munro (1989, 1999).The local coordinates are relative to the NE corner marker of site A (Fig 1).
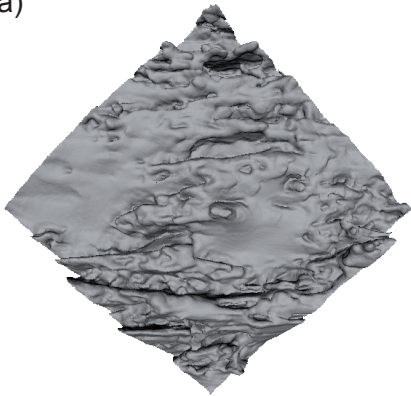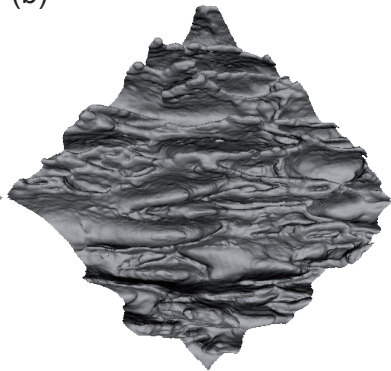
Figure ~~9~~10: Wind rose for the whole study period (26 Nov 2013 – 3 Jan 2014).

~~Figure 10: Comparison of surface height through time extracted from the Kinect scan and measured manually along the horizontal reference. Error ranges on the Kinect cross profiles are given by a linear interpolation of total positional error between the bounding stakes. Solid black triangles indicate locations where snowdepth exceeded the length of the 3 m probe.~~
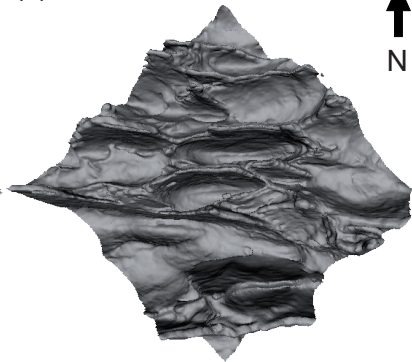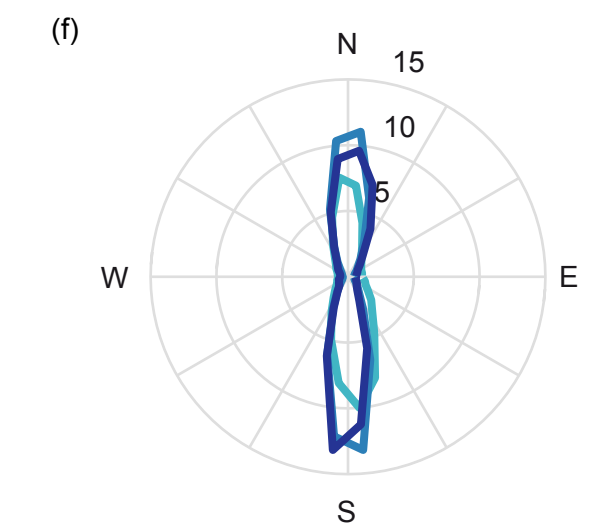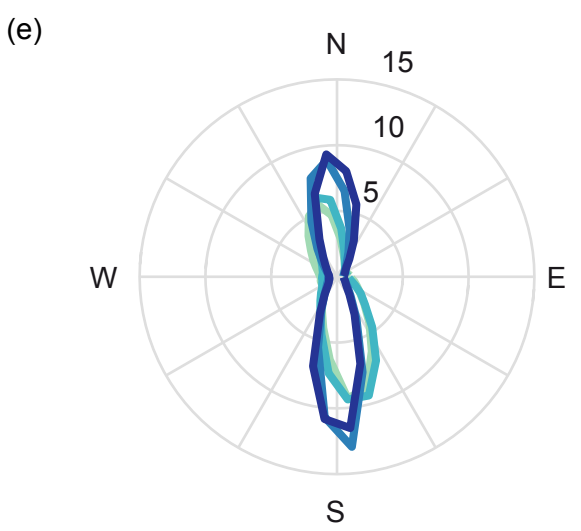
(a)

B

AWS

A

0 1 2 m

(b)

GPS base
Test site
AWS
Glacier site

0   280   560 m

(a)   (b)   absolute distances [mm]

50

25

0

(a) (b) (c)

	25-Nov	11-Dec	20-Dec	03-Jan
mean height [m]	-1.00	-1.35	-1.69	-2.66
height range [m]	1.14	0.86	1.22	1.60
surface [m²]	15.04	13.13	12.13	27.95
surface/area	2.15	1.88	1.73	3.99

	25-Nov	11-Dec	20-Dec	03-Jan
mean height [m]		0.19	-0.30	-1.13
height range [m]		0.61	0.99	1.11
surface [m²]		4.73	8.42	7.79
surface/area		2.10	3.74	3.46
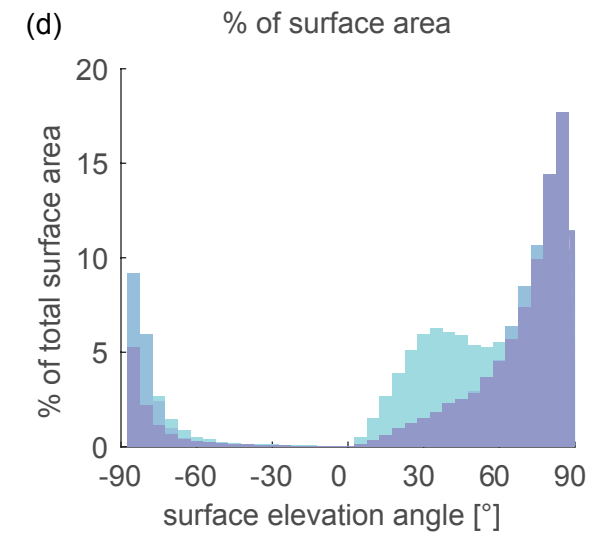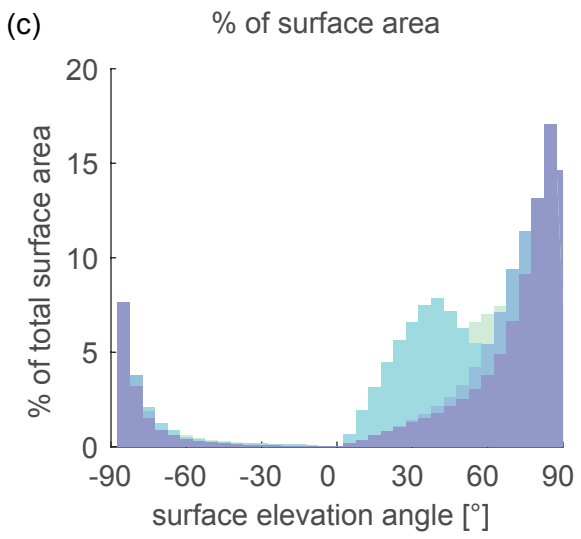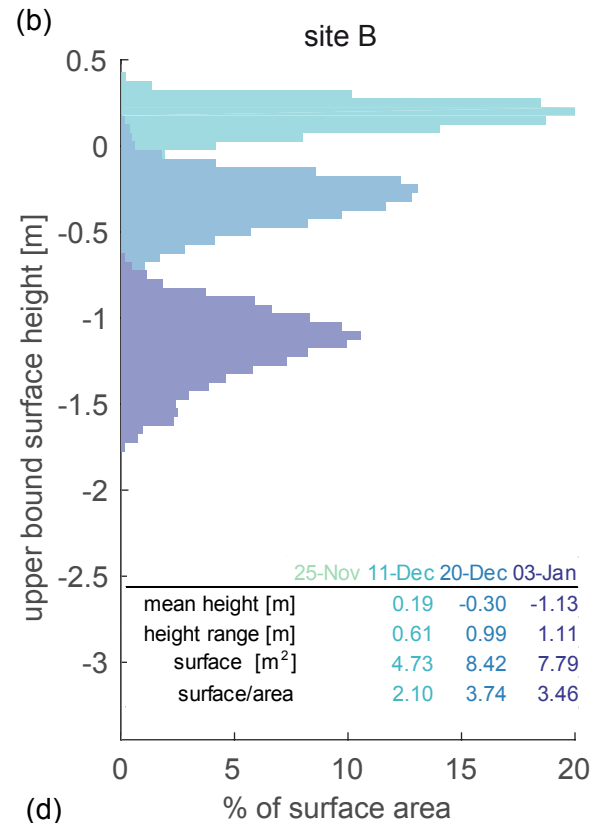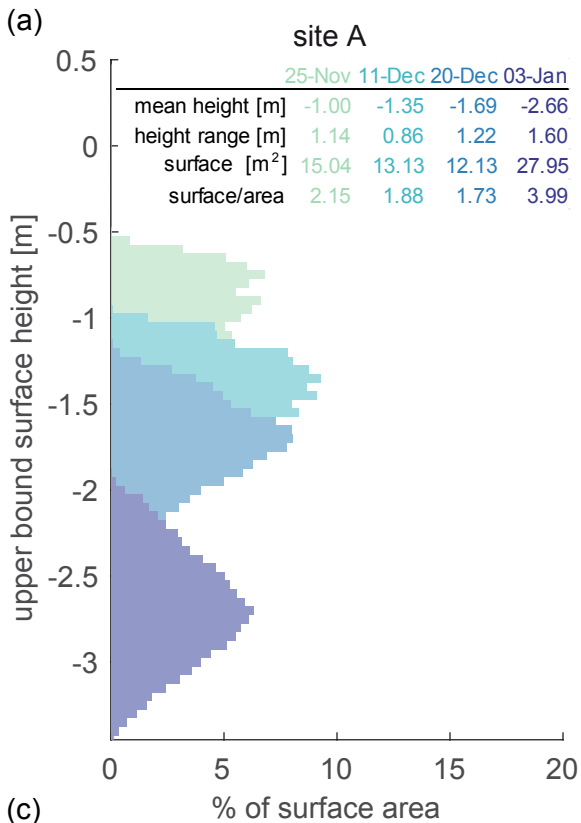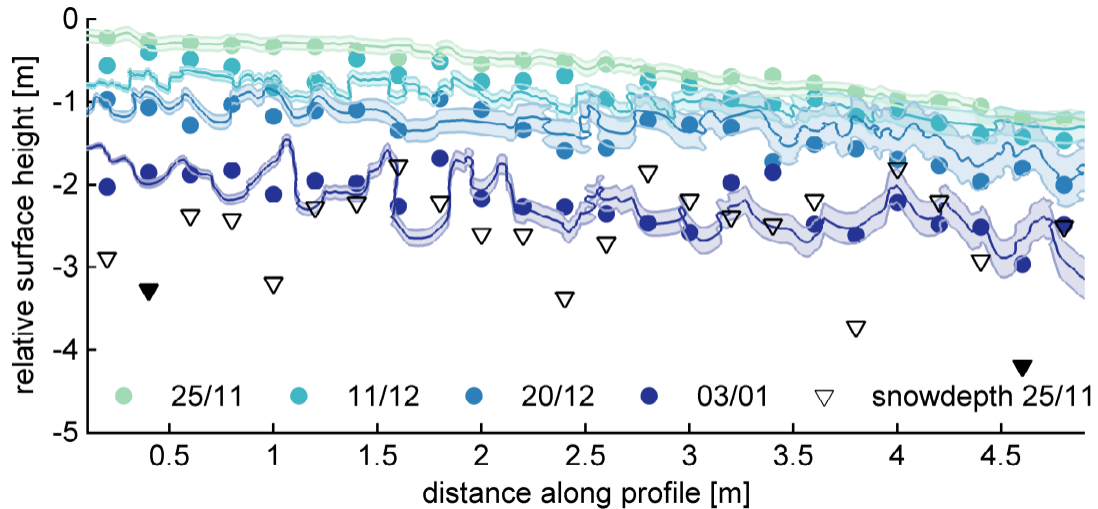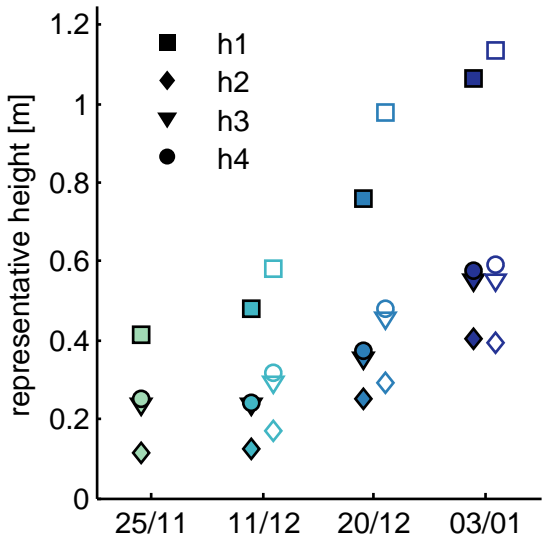
site A
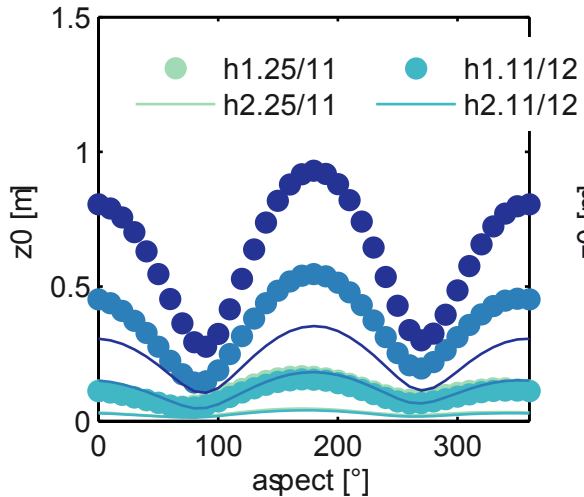
site B
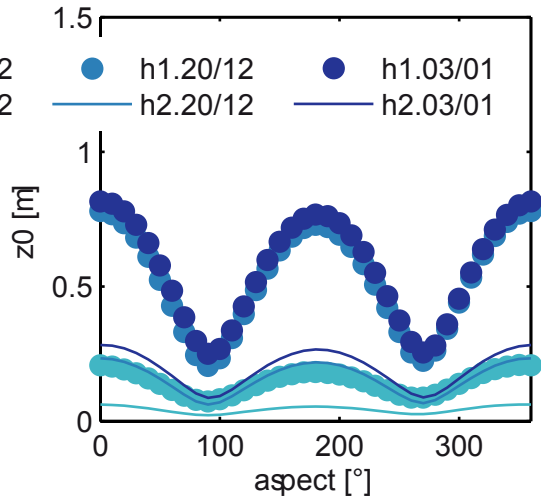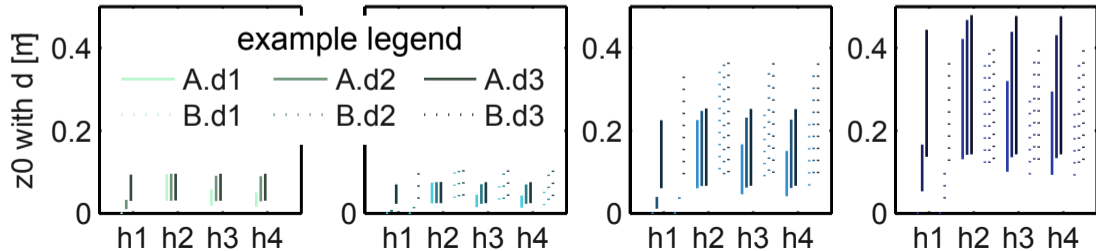
N−S sections >1.5m	E−W sections > 1.5m

11/12

20/12
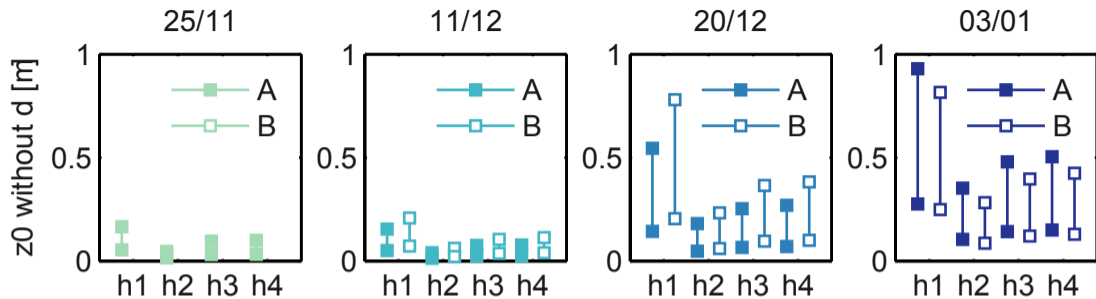
03/01

26.11.13 − 03.01.2014

NORTH

8%

4%

WEST

EAST

SOUTH

[m s⁻¹]
7 − 8
6 − 7
5 − 6
4 − 5
3 − 4
2 − 3
1 − 2
0 − 1
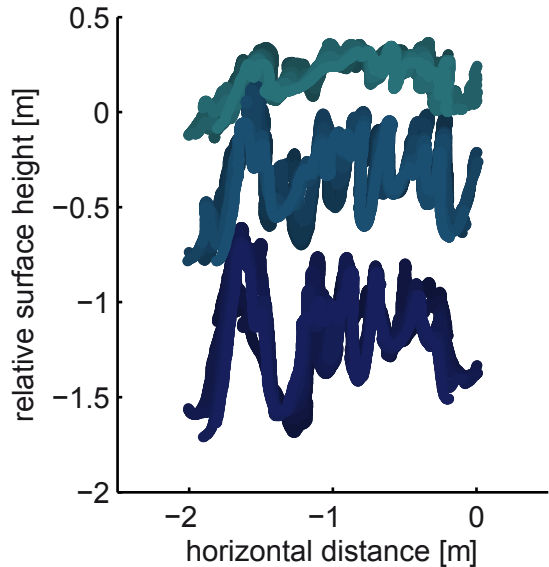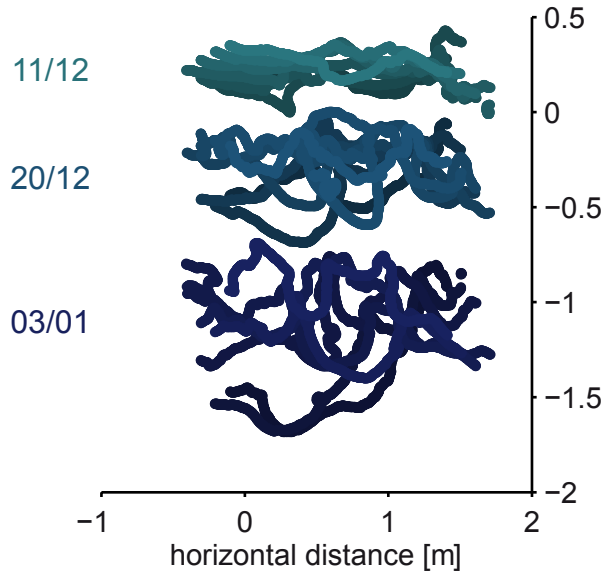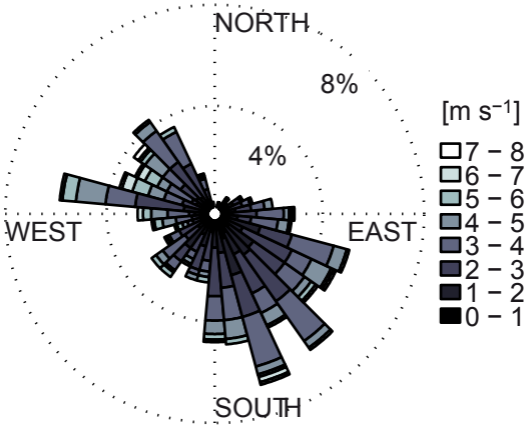
A: GPS positions of the base of the marker stakes for sites A and B in UTM region 19S, using the WGS84 datum and ww15mgh geoid, showing combined XY, and XYZ standard deviations (std) are less than 2 cm for all stakes.

	easting	std easting	northing	std northing	elevation	std elevation	XY std [mm]	XYZ std [mm]
SA-1	410909.704	0.004	6664147.933	0.007	4774.568	0.015	8	17
SA-2	410910.615	0.006	6664143.153	0.011	4773.496	0.008	13	15
SA-3	410908.618	0.004	6664142.623	0.004	4773.375	0.013	6	14
SA-4	410907.751	0.004	6664147.731	0.003	4774.518	0.015	5	16
SA-5	410908.046	0.004	6664145.189	0.003	4773.988	0.017	5	18
SB-1	410911.808	0.005	6664156.396	0.007	4775.352	0.014	9	16
SB-2	410913.034	0.004	6664154.925	0.011	4775.278	0.012	12	17
SB-3	410911.426	0.003	6664153.732	0.003	4775.314	0.011	4	12
SB-4	410910.228	0.003	6664155.065	0.004	4775.464	0.011	5	12

B1: Information on the mesh components and alignment errors for each scanned surface at both glacier sites.

	Site A				Site B		
	25-Nov	**11-Dec**	**20-Dec**	**03-Jan**	**11-Dec**	**20-Dec**	**03-Jan**
# of meshes used	13	10	13	10	6	6	3
# of arcs used (potential arcs)	16(28)	16(21)	17(28)	11(19)	9	11	5
mean error [mm]	2.396	2.632	2.995	3.171	2.524	3.241	3.484
median error [mm]	2.172	2.541	3.112	2.945	2.414	3.310	3.285
90th % error [mm]	3.186	3.541	3.567	3.836	2.784	3.781	3.386

B2: Detailed mesh-processing procedure used in this study.

- All processsesing was carried out in Meshlab unsless otherwise stated
- Pairwise point alignment of the component surface meshes covering each study site
- Applied filter to remove mesh sections (vertices and faces) consisting of < XXX vertices
- Applied filter to remove unreferenced and duplicated vertices
- ICP alignment optimization of the mosaicked component surface meshes using the following parameters:
    - sample number of 1000 for each ICP iteration
    - minimal starting distance for chosen points of 10 mm at the first iteration reducing by 20% on each iteration
    - maximum of 50 iterations were performed
    - using rigid matching so that no stretching or warping of the mesh is permitted
    - export distributed alignment error
- Flattened mosaicked surface meshes into a single layer and remeshed using a Poisson filter with the following paramters:
    - Octreee depth (12)
    - Solver divide (7)
    - number of samples per node (1)
- Meshes were georeferenced with differential GPS measurements in Polywork
- Corner marker stakes, and parts of the mesh representing sensors installed within the sample site were manually removed from the georeferenced surface mesh and the mesh was cropped at the margins
- Triangle numbers were reduced by merging vertices closer than 2.5mm
- Resultant non-manifold features were removed
- Closed holes using a 20mm diameter filter. Inspected boundaries of resultant meshes to confirm that all remaining boundaries are on the edges of the sub-sampled area.
- Cropped horizontal areas to a consistent patch size: A 2 x 3.5m; B 1.5 x 1.5m
- Exported as .OBJ file from which the vertex coordinates and face indices and metadata were extracted for subsequent analysis in Matlab.

C: Comments and recommendations on the Kinect sampling strategy used in this study.

- Daylight swamps the signal of the Kinect. Over rock surfaces the Kinect worked perfectly as long as the surface was not in direct sunlight. Over snow and ice the effective range was reduced to about 1m and scanning could only be performed once the sun was below the horizon and was even better after darkness had fallen.
- This study used ReconstructMe as the capture software as it performs real time meashing so that the quality of the surface collected can be assessed at the time of capture. This is an advantage for:
    - observing if return signals had been obtained from the troughs of the penitentes as penetration into very narrow penitente troughs was only achieved over several passes and by re-orientating the sensor to be parallel with the trough.
- The disadvantages of ReconstructMe are that:
    - it does not save the raw depth data
    - it requires a computer with a powerful graphics processor as the real time processing is performed at the same 30Hz frequency as the depth-map frame production of the Kinect.
    - the powerful graphics processor tends to be power hungry
- Alternative systems for sampling Kinect data are numerous and growing, and the user must do some up to date research to discover the newest developments, but some existing options are to:
    - use the 'KinectFusion' algorithm (Izadi et al., 2011;Newcombe et al., 2011), implemented in the 'Kinfu' program (part of the Point Cloud Library (PCL); Rusu and Cousins, 2011), which allows one to move the Kinect and scan an area or object, automatically stitching together each frame into one large 3D model, while also capturing raw data.
    - for very large areas, the Kinfu implementation has been extended, named Kintinuous, and used to map paths more than 100m long (Whelan et al., 2012).
- When covering an area larger than 1m² with a Kinect survey it would be advantageous to have a camera boom mounting for moving the Kinect smoothly over the glacier surface, as this would mean larger areas can be scanned in a single mesh. This would save significant work, and additional error involved in aligning and mosaicking the meshes.
- Ground control point markers which have fixed geometric surfaces with known alignment to x, y, z would have facilitated the alignment and mosaicking the component meshes of each scan. On the basis of this study a marker pole with cubes attached to it at fixed heights and known orientations would be ideal. As the surface lowers and more of the marker stake is revealed additional markers should be added at known distances below the previous marker cube.
- A higher number of ground control points to provide redundancy is advisable as in the case of poorly represented locations for georeferencing step, these could be excluded and the remaining points would still allow successful georeferencing.